NONEQUILIBRIUM HYPERSONIC FLOWS
& HYPERSONIC NOZZLE FLOW MODELING

Graham V. Candler

Department of Aerospace Engineering and Mechanics

University of Minnesota, Minneapolis, MN 55455.

1. Introduction

These notes are arranged in the following manner. In the introduction section, we use several examples to illustrate some of the issues that must be addressed when we model hypersonic flows. This leads to a discussion of what types of computational fluid dynamics methods are suitable for these flows. Then the conservation equations for a mixture of chemically reacting and weakly ionized gases is developed. We discuss the thermochemistry models and the relevant boundary conditions for these flows. Then in the third section, computational fluid dynamics methods for these flows are discussed. We analyze the conservation equations, and discuss an upwind method. Then, the integration of the source terms is discussed. In the fourth section we discuss several advanced topics in the modeling of hypersonic flows. Finally, we discuss specific application to hypersonic nozzle flow analysis.

1.1 Examples of Hypersonic Flows

In this subsection, we discuss a few external hypersonic flows to illustrate some of the issues that we must address when the flow field is chemically reacting. These examples show that aerothermochemistry can have a major impact on aerodynamic coefficients, heat transfer rates, and radiative emission from hypersonic flows.

1.1.1 Hypersonic Double-Cone Flow

An interesting flow field is created by a double-cone geometry. Figure 1.1 plots a schematic of this flow field for an approximately Mach 12 free-stream condition. Note the attached shock wave that originates at the first cone tip, the detached shock wave formed by the second cone, and the resulting shock triple point. The transmitted shock impinges

on the second cone surface, which separates the flow and produces a large localized increase in the pressure and heat transfer rate. This pressure rise causes the flow to separate, and also produces a supersonic under-expanded jet that flows downstream near the second cone surface. The size of the separation zone depends strongly on the location and strength of the shock impingement. This flow field is very sensitive to the wind tunnel conditions, the physical models used in the CFD code, and the quality of the numerical methods used to predict the flow (Ref. 58).
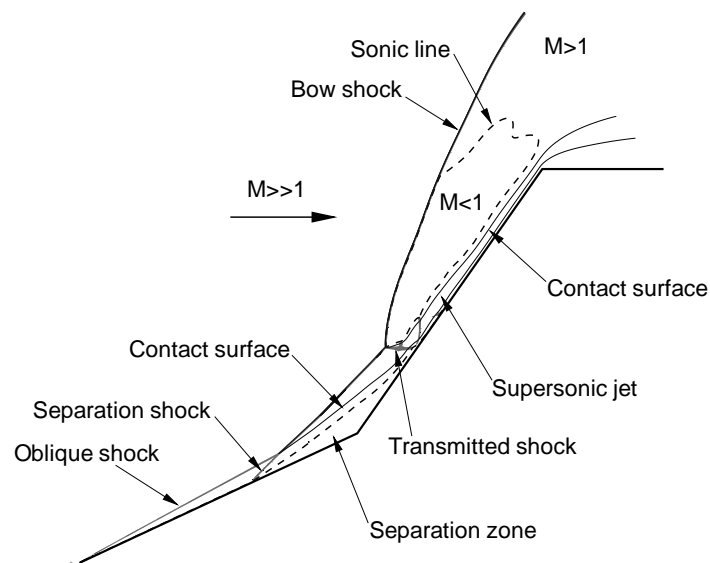

Figure 1.1 – *Schematic of the hypersonic double-cone flow field.*

Experiments on the double-cone have been performed at hypersonic conditions in the CUBRC Large Energy National Shock Tunnel (LENS). These experiments used a large model with many surface-mounted heat flux and pressure transducers (Ref. 31). Nitrogen was used as the test gas to minimize the effects of chemical reactions, and the experiments were done at low density to ensure laminar boundary layers and shear layers. This dataset was the subject of a blind code validation study. In general, the comparison between simulation and experiment was shown to be quite good, however there were several important differences. Interestingly, the simulations performed with high-quality numerical methods on the finest grids slightly over-predicted the size of the separation zone, and all simulations predicted excessive heating in the attached region prior to separation (Ref. 31). This is shown in Fig. 1.2, which presents typical results for two double-cone cases. The error on the first cone is as much as 20%, which is particularly puzzling because the pressure is accurately predicted in this region. Many attempts were made to explain this

difference by running CFD cases with extreme grid resolution, finite nose-tip bluntness, model misalignment, and uncertainties in reaction rates. None of these effects was found to explain the differences shown in Fig. 1.2.
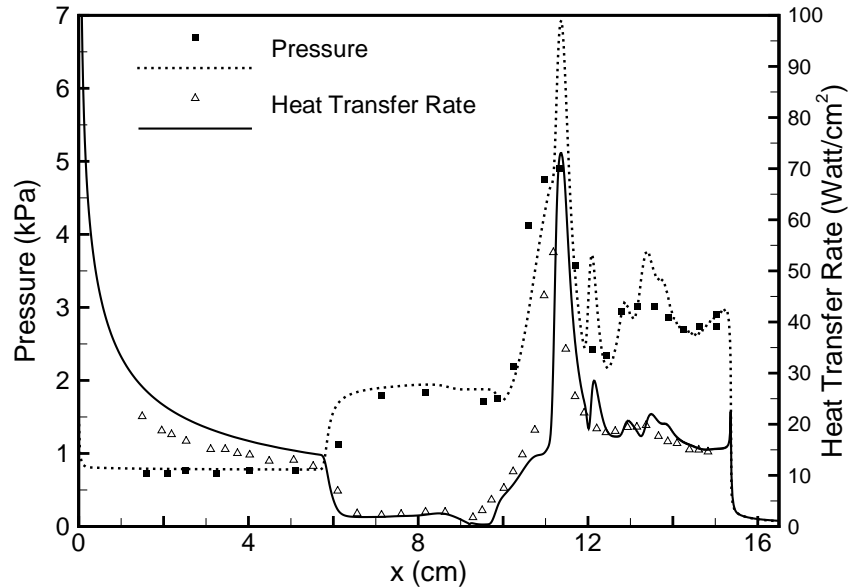

Figure 1.2 – *Comparison of predicted and measured surface pressure and heat flux on the double cone model. Ref. 31.*
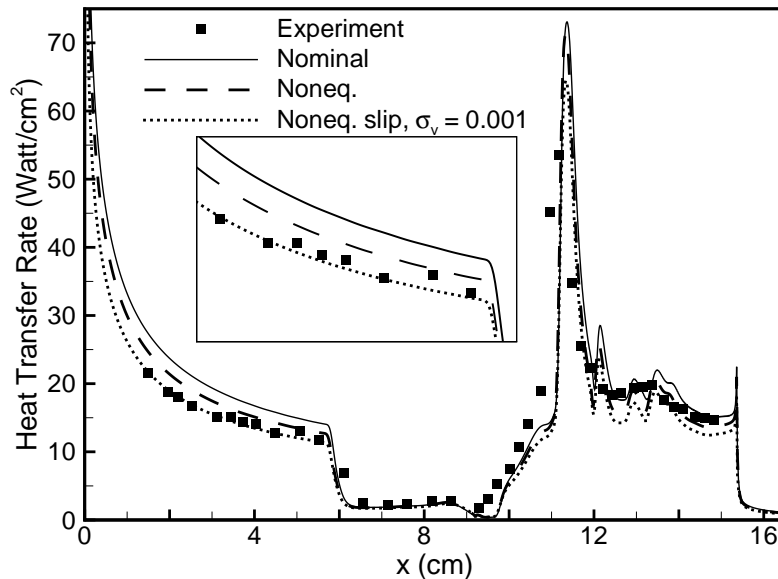

Figure 1.3 – *Comparison of measured double cone heat flux and different models for the effects of nonequilibrium vibrational energy. 'Nominal' is the baseline model (Fig. 1.2); 'Noneq.' is accounting for vibrational nonequilibrium in the free-stream; and 'Noneq. Slip' also includes the effect of imperfect accommodation of vibrational energy to the surface.*

The specification of the free-stream conditions in a hypersonic shock tunnel can be difficult because these facilities may be subject to non-ideal effects in the nozzle. Namely, a reflected shock wave is used to heat and compress the test gas to extremely high pressure and temperature, which results in vibrational excitation and chemical reaction. Then the test gas rapidly expands through the nozzle, and its internal energy state may not fully de-excite during the expansion. As a result, the gas flowing over the model may be in a non-ideal thermo-chemical state. The double-cone experiments were run with nitrogen at moderate enthalpy ($h_0 < 4\,\mathrm{MJ/kg}$); this results in virtually no chemical reaction, but vibrational excitation of the gas in the reflected shock region. Nitrogen vibrational modes relax very slowly, and for these test conditions this results in elevated vibrational energy in the wind-tunnel test section. A vibrational finite-rate simulation of the nozzle flow shows that the vibrational energy modes are frozen near the throat temperature ($T_v = 2560\,\mathrm{K}$). This has two major effects: the kinetic energy flux is reduced by about 10%, and because nitrogen vibrational energy modes are inefficient at accommodating to most metallic surfaces, they do not transfer their energy to the model. These two effects reduce the heat flux by about 20%, and significantly improve the comparison between CFD and experiment; this is shown in Fig. 1.3 (Ref. 58).

1.1.2 Mars Science Laboratory Entry

During the past 30 years or so, great strides have been made in the simulation of atmospheric entry flows. In part, this is a result of increases in computer power and the development of efficient parallel codes for solving the governing equations. Recently, unstructured grids have begun to be used for difficult aerothermodynamics problems. Interestingly, however almost no research has been done on improving the governing equations used in these simulations. Thus, we are solving essentially the same equations now as when the first CFD simulations of nonequilibrium atmospheric entry flows were performed. Furthermore, current codes are often used far beyond the range of conditions for which they have been validated.

Figure 1.4 illustrates a recent simulation of the flow over the Mars Science Laboratory (MSL) capsule at Mach 18.1 (Ref. 71), with the flow in the wake region represented by the detached eddy simulation (DES) approach (Ref. 78) with the Spalart-Allmaras one-equation turbulence model (Ref. 77) and the Catris and Aupoix (Ref. 11) compressibility correction. This simulation used finite-rate kinetics to represent the Mars atmosphere and was performed on 16 million element hybrid unstructured grid. Not shown in this image is that the operation of the reaction control system thrusters is also modeled in this

simulation. With current parallel clusters, such a calculation can be performed at useful turn-around times. (The base flow is established in about half a day, and the operation of the RCS thrusters is computed and averaged over an additional two days on 240 cores of an SGI Altix SE 1300 cluster.)
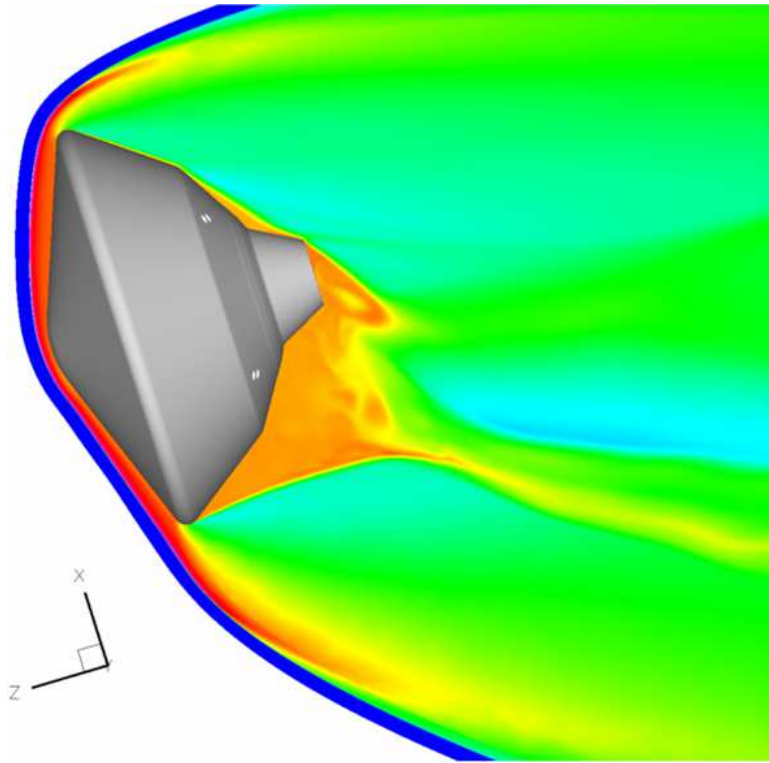

Figure 1.4 – *Temperature contours in the flow field of the MSL capsule at Mach 18.1 conditions.*

1.2 Important Effects

1.2.1 Thermochemical Nonequilibrium

A gas is in thermal nonequilibrium if its internal energy cannot be characterized by a single temperature, and it is in chemical nonequilibrium if its chemical state does not satisfy chemical equilibrium conditions. Portions of many external hypersonic flows are in thermal and chemical nonequilibrium. This occurs because as the gas passes through the bow shock wave, much of its kinetic energy is converted to random translational motion. Then, collisions transfer translational energy to rotational, vibrational, electronic, and chemical energy. This energy transfer takes a certain number of collisions, during which time the gas moves to a new location where the temperature and density may be different.

Thus, the internal energy modes and chemical composition of the gas lag the changes in the translational temperature. We can determine if a flow will be in thermal or chemical nonequilibrium by constructing the Damköhler number, Da, which is the ratio of the fluid motion time scale to the internal energy relaxation or chemical reaction time scale.

Consider the steady-state mass conservation equation for species s

$$\frac{\partial}{\partial x_j}\left(\rho_s u_j\right) = w_s, \tag{1.1}$$

where ρ_s is the mass density of species s, u_j is the gas velocity in the x_j direction, and w_s is the rate of production of species s per unit volume due to chemical reactions. We can non-dimensionalize this equation using the total density, ρ, the speed, V, and a relevant length scale such as the nose radius, r_n. Then

$$\frac{\partial}{\partial \bar{x}_j}\left(\bar{\rho}_s \bar{u}_j\right) = \frac{r_n w_s}{\rho V} = \frac{\tau_f}{\tau_c} = Da. \tag{1.2}$$

Thus, Da represents the ratio of the fluid motion time scale, τ_f, to the chemical reaction time scale, τ_c; or it is the ratio of the chemical reaction rate to the fluid motion rate. A similar expression can be derived to describe the relative rate of internal energy relaxation.

When $Da \to \infty$, the internal energy relaxation or chemical reaction time scale approaches zero (becomes infinitely fast), and the gas is in equilibrium. That is, its thermal or chemical state adjusts instantaneously to changes in the flow. When $Da \to 0$, the reaction time scale approaches infinity, the gas is frozen and does not adjust to changes in the flow. The Damköhler number is useful for determining how reactive the gas is, and what type of analysis is appropriate for given flow conditions.

When the chemical source term, w_s, is proportional to the density squared (as it is for dissociation reactions), the binary scaling law can be derived from the above expression. Let us write $w_s = C\rho^2 k_f$, where k_f is a temperature-dependent reaction rate, and C is a constant. Then we have

$$Da = \rho\, r_n \frac{C k_f}{V}. \tag{1.3}$$

Thus, the reaction rate is proportional to the density-length scale product. k_f depends exponentially on temperature, which for hypersonic flows depends on the free-stream kinetic energy $\frac{1}{2}V_\infty^2$. Therefore, for a dissociation-dominated flow, the Damköhler number depends on the binary scaling parameter, $\rho\, r_n$, and the free-stream kinetic energy.

1.2.2 Vibration-Dissociation Coupling

When a gas becomes vibrationally excited, the population of the excited vibrational states increases. As shown in Fig. 1.5, this decreases the energy required to dissociate the molecule. Therefore, the vibrational state of a molecule affects its dissociation rate. This process is not fully understood, and simple models that can be implemented in computational methods are largely unvalidated. Even small changes in the dissociation rate can change the flow field considerably and can lead to uncertainties in the trim angle of attack of hypersonic vehicles.

There are many models available for the vibration-dissociation process, and we will discuss the most popular models in these notes.
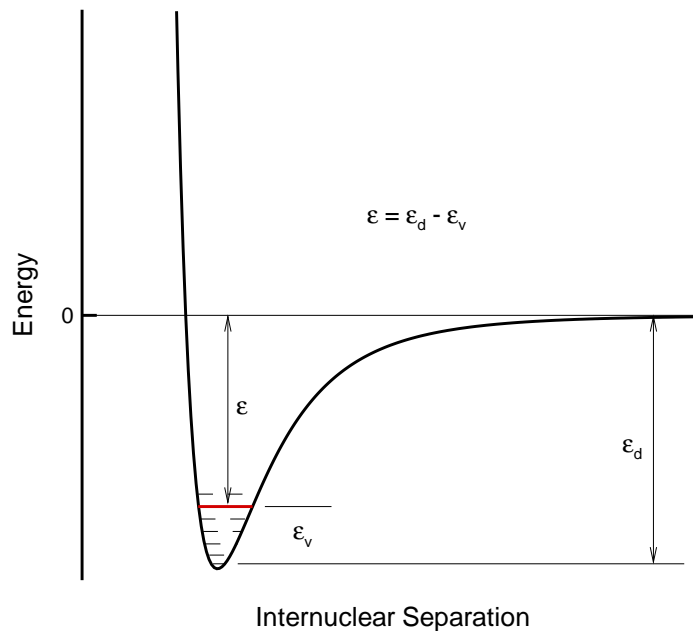

Figure 1.5 – *Schematic of the vibrational state of a molecule and the energy required for dissociation.*

1.2.3 Finite-Rate Wall Catalysis

One of the most important parameters that determines the convective heat transfer rate for hypersonic vehicles is the surface catalytic efficiency. Fay and Riddell (Ref. 18) used a self-similar stagnation point boundary layer analysis to show that depending on the

reactivity (Damköhler number) of the boundary layer and the catalytic efficiency of the surface, the heat transfer rate is dramatically changed. As seen in Fig. 1.6, if the boundary layer is frozen ($Da \to 0$) and the body surface is noncatalytic, the heat transfer rate may be reduced by 50% or more, depending on the fraction of energy tied up in the chemical energy modes.
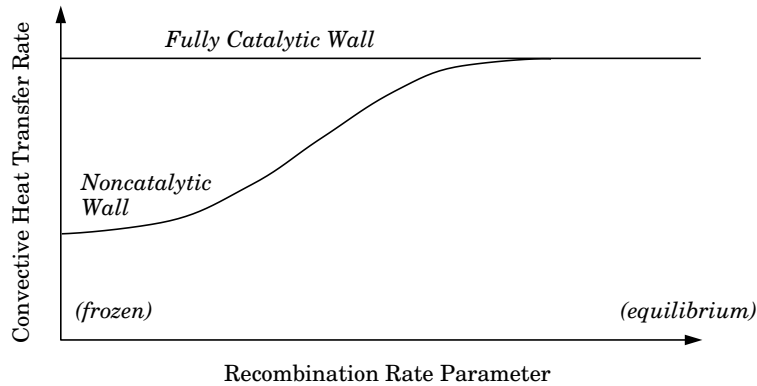

Figure 1.6 – *Effect of wall catalysis on convective heat transfer rate at a stagnation point. (After Fay and Riddell (Ref. 18).)*

When the wall is noncatalytic, it does not promote recombination at the surface. Thus, if the reaction rate is slow near the surface, a fraction of the total energy of the gas remains in the form of chemical energy. Thus, it does not contribute the convective heating. If, on the other hand, the surface is catalytic or the boundary layer is near equilibrium, the chemical energy is released at the vehicle surface, and the heat transfer increases.

It is important to note how the chemical reactions scale with density. As we saw in the previous section, dissociation scales with the binary scaling parameter, $\rho\,r_n$. However, recombination is a three-body process, and as a result scales with ρ^2. Thus, in typical low-density atmospheric entry conditions, recombination may be very slow relative to dissociation. The surface reactions typically scale differently because they are usually diffusion limited and depend strongly on the surface material properties.

1.2.4 Nonequilibrium Thermal Radiation

The modeling of thermal radiation from the flow field remains a major challenge. The difficulty arises because the radiative emission from the gas depends very strongly on its internal energy. For example, immediately behind the bow shock wave in the stagnation region of a vehicle, the vibrational temperature may overshoot the equilibrium post-shock temperature. Then, if the population of the excited electronic states of the gas is governed

by the vibrational temperature, there is a dramatic super-equilibrium population of the excited electronic states. The excited electronic states decay to the ground state, and the electronic energy is emitted as photons (thermal radiation), many of which are absorbed by the body surface. Thus, for high-energy flows where radiative heating is important, there may be a significant increase in the heat transfer rate due to nonequilibrium. This process is very difficult to model because there are many complicated rate-dependent processes competing for the thermal energy produced by the shock wave.

1.2.5 Low Density Effects

During re-entry many hypersonic vehicles spend a significant time at high altitude where the gas dynamics are poorly understood. In this high Knudsen number regime, the bow shock wave thickness becomes an appreciable fraction of the shock standoff distance, none of the internal energy modes are in equilibrium with the translational modes, and there is velocity and temperature slip at the body surface. Also, the chemical reactions may not conform to standard reaction rate models and the vibration-dissociation coupling effects are very important. Good progress has been made in the modeling of each these effects (Refs. 5, 22, 48). However, in extremely low density flows, the continuum formulation completely breaks down and a particle based simulation method must be used (such as the direct simulation Monte Carlo method (Ref. 2)).

1.2.6 Other Effects

Many other complicated phenomena may occur in hypersonic external flows. For example, at low-earth-orbit re-entry speeds and above, the flow field becomes ionized and the radio frequency transmissions may be blacked out. At higher speeds, the vehicle surface must be ablative to protect the vehicle from heating. In this case, foreign species are injected into the flow field, where they react with the air species to form other chemical species. Thirdly, shock-wave boundary layer interactions are very complicated and intense at hypersonic conditions. Finally, of course, there is the question of transition to turbulence. If the boundary layer is turbulent, the convective heat transfer rate to small-angle bodies (blunted cones, for example) increases by a factor of between three and eight. There are no reliable models for transition at hypersonic Mach numbers, and the effect of boundary layer chemical reactions on transition is poorly understood. However, it has been shown experimentally and with stability theory that endothermic (energy absorbing) reactions tend to delay transition in hypersonic boundary layers (Ref. 33). Reynolds-averaged Navier-Stokes (RANS) models are largely unproven at hypersonic conditions.

1.3 Computational Methods

From the previous discussion, it is clear that there are many difficult issues that must be addressed. Hypersonic flows may have one or more of the following features:

1. A large number of chemical species reacting with one another at a wide range of relative time scales.

2. Complicated interactions between the fluid motion, internal energy state, and the chemical composition of the gas.

3. Length scales ranging from the characteristic length of the body down to the shock wave thickness.

4. Complex gas-surface interactions, including slip at the wall, foreign species injection, and finite-rate catalysis of reactions at the surface.

5. Transitional and turbulent boundary layers.

A numerical method that can solve the equations that describe these flows must have certain qualities. Generally, we are interested in steady-state flows. Also, many flows have regions of very high reaction rate, making the range of time and length scales very large. Thus, it is essential to use an implicit method for at least the chemical reaction terms. Also, the computational and memory costs of the method should not increase too quickly with the number of chemical species being considered. Finally, to solve very large and difficult problems, it is mandatory that the method run efficiently on parallel computers.

2. Conservation Equations

2.1 Assumptions

We assume that the gas is described by the Navier-Stokes equations extended to account for the presence of chemical reactions and internal energy relaxation. For these equations to be valid, the flow must satisfy the following criteria:

1. The gas must be a continuum. If we relate the mean-free-path, λ, to a local length scale that is determined by the normalized density gradient, we can form the gradient-length-local Knudsen number as (Ref. 4):

$$(\text{Kn})_{\text{GLL}} = \frac{\lambda}{\rho} \left| \frac{d\rho}{d\ell} \right|, \tag{2.1}$$

where ℓ is in the direction of the steepest density gradient. Boyd, *et. al* (Ref. 4) showed that when $(\text{Kn})_{\text{GLL}} > 0.05$ the Navier-Stokes formulation fails.[1] This typically occurs in shock waves and near the body surface in low density flows. Also, the wake region of blunt bodies may have regions of continuum formulation failure. In these regions, either a higher-order continuum formulation must be used (Refs. 48, 91) or a particle-based method such as the direct simulation Monte Carlo (DSMC) method is required.

2. The mass diffusion fluxes, shear stresses, and heat fluxes must be proportional to the first derivatives of the flow quantities. If not, a non-continuum approach, such as the direct simulation Monte Carlo (DSMC) method must be used.[2]

3. The internal energy modes must be separable. That is, we can describe each energy mode by its own temperature. For example, the energy contained within the vibrational modes cannot be a function of the rotational energy state.

4. Finally, the flow is only weakly ionized. In this case, the Coulomb cross-section is small relative to the electron-neutral collision cross-section.

---

[1] In this work, failure was defined to occur when the Navier-Stokes solution differs by 5% from the results obtained using the direct simulation Monte Carlo method.

[2] Some authors advocate the use of higher-order continuum equations such as the Burnett equations (Ref. 6). However, there is an inherent problem with using this approach. The continuum equations fail because the velocity distribution function becomes highly non-Maxwellian, or even a bi-modal mixture of perturbed Maxwellians. No perturbation to a single Maxwellian can represent such a bi-modal velocity distribution function. Thus, an approach based on higher-order perturbations to a single equilibrium velocity distribution function cannot work.

2.2 Governing Equations

In this section the governing equations are given; further information on their derivation can be found in Refs. 10, 21, 41, 64, and 65. We will discuss the derivation of the vibrational energy equation in some detail because it provides a good example of how to derive conservation equations for nonequilibrium flows. Also this derivation will show the strong interaction between the vibrational state and the chemical reactions in a nonequilibrium gas.

2.2.1 Mass Conservation

The mass conservation equation for species s is:

$$\frac{\partial \rho_s}{\partial t} + \frac{\partial}{\partial x_j}\left(\rho_s u_j + \rho_s v_{sj}\right) = w_s, \tag{2.2}$$

where again, ρ_s is the species density and w_s is the chemical source term. The mass-averaged velocity is u_j and the diffusion velocity of species s is v_{sj} in the x_j direction. The mass-averaged velocity is obtained using:

$$u_j = \sum_{s=1}^{ns} \frac{\rho_s}{\rho} u_{sj}, \qquad \rho = \sum_{s=1}^{ns} \rho_s, \tag{2.3}$$

where ns is the number of chemical species. The diffusion velocity is the velocity of species s, u_{sj}, relative to the mass-averaged velocity:

$$v_{sj} = u_{sj} - u_j. \tag{2.4}$$

2.2.2 Momentum Conservation

The momentum equation has the familiar form except for the presence of the electric field, $\tilde{E}_i$:

$$\frac{\partial}{\partial t}\left(\rho u_i\right) + \frac{\partial}{\partial x_j}\left(\rho u_i u_j + p\delta_{ij} - \tau_{ij}\right) = \sum_{s=1}^{ns} e Z_s N_s \tilde{E}_i, \tag{2.5}$$

where $e Z_s$ is the charge of species s and N_s is the species number density. The pressure p is the sum of the partial pressures:

$$p = \sum_{s=1}^{ns} p_s = \sum_{s=1}^{ns} \rho_s \frac{R}{M_s} T, \tag{2.6}$$

where R is the universal gas constant and M_s is the molecular weight of species s. T is the translational temperature of the gas mixture. The expression for the shear stress will be given below.

2.2.3 Total Energy Conservation

The total energy conservation equation has the form:

$$\frac{\partial E}{\partial t} + \frac{\partial}{\partial x_j}\left((E+p)u_j - \tau_{ij}u_i + q_j + \sum_{s=1}^{ns}\rho_s v_{sj}h_s\right) = \sum_{s=1}^{ns} eN_s Z_s \tilde{E}_i u_i, \qquad (2.7)$$

where E is the total energy per unit volume, q_j is the total heat flux vector, and h_s is the species s specific enthalpy. These quantities will be discussed in more detail below.

2.2.4 Vibrational Energy Conservation

The derivation of the vibrational energy conservation equation is non-trivial because the vibrational state is coupled to the chemical state. As we discussed in Section 1.2.2, molecules that are highly vibrationally excited are more likely to dissociate than the average molecule. Thus, when dissociation occurs, the process removes more than the average vibrational energy from the vibrational energy pool. Likewise, when recombination occurs the newly formed molecule may be formed at an elevated vibrational level. A complete derivation of this equation is available in Ref. 60.

We assume that there is a single diatomic species in a multi-species gas mixture. In a manner similar to Clarke and McChesney (Ref. 14), we let $f_{s_\alpha}(x_i, v_{s_\alpha}, t)\,dx\,dv_{s_\alpha}$ represent the number of particles in vibrational level α of species s in a volume $dx \equiv dx_1\,dx_2\,dx_3$ and $dv_{s_\alpha} \equiv dv_{s_{\alpha_1}}\,dv_{2_{\alpha_2}}\,dv_{s_{\alpha_3}}$. The velocity distribution function f_{s_α} is defined such that

$$\int_{-\infty}^{+\infty} f_{s_\alpha}\,dv_{s_\alpha} = n_{s_\alpha}, \qquad (2.8)$$

where n_{s_α} is the number density of molecules in level α of species s.

Under the assumption that the translational energy is a classical energy mode and that all velocities in the range $-\infty$ to $+\infty$ are allowed, we can show that f_{s_α} obeys the Boltzmann equation:

$$\frac{\partial f_{s_\alpha}}{\partial t} + v_{s_{\alpha_i}}\frac{\partial f_{s_\alpha}}{\partial x_i} + F_{s_{\alpha_i}}\frac{\partial f_{s_\alpha}}{\partial v_{s_{\alpha_i}}} = C_{s_\alpha}^+ - C_{s_\alpha}^-, \qquad (2.9)$$

where $F_{s_{\alpha_i}}$ is the external force per unit mass acting in the i direction on the particles, and $C_{s_\alpha}^+$ and $C_{s_\alpha}^-$ represent the number of particles created and destroyed due to collisions of species s in level α per unit time and per unit phase space volume. These terms, $C_{s_\alpha}^+$ and $C_{s_\alpha}^-$, are the collision integrals.

The conservation of vibrational energy equation for species s is found by taking the moment of the Boltzmann equation with respect to ϵ_{s_α} and summing over all vibrational energy levels α. This yields

$$\sum_\alpha \int_{-\infty}^{\infty} \epsilon_{s_\alpha} \frac{\partial f_{s_\alpha}}{\partial t}\, dv_{s_\alpha} + \sum_\alpha \int_{-\infty}^{\infty} \epsilon_{s_\alpha} v_{s_{\alpha_i}} \frac{\partial f_{s_\alpha}}{\partial x_i}\, dv_{s_\alpha}$$
$$+ \sum_\alpha \int_{-\infty}^{\infty} \epsilon_{s_\alpha} F_{s_{\alpha_i}} \frac{\partial f_{s_\alpha}}{\partial v_{s_{\alpha_i}}}\, dv_{s_\alpha} = \sum_\alpha \int_{-\infty}^{\infty} \epsilon_{s_\alpha} (C_{s_\alpha}^+ - C_{s_\alpha}^-)\, dv_{s_\alpha}. \qquad (2.10)$$

where ϵ_{s_α} is the amount of vibrational energy per molecule of species s in level α.

The convection term on the left hand side of (2.10) can be manipulated to yield

$$\sum_\alpha \int_{-\infty}^{\infty} \epsilon_{s_\alpha} v_{s_{\alpha_i}} \frac{\partial f_{s_\alpha}}{\partial x_i}\, dv_{s_\alpha} = \frac{\partial q_{vsi}}{\partial x_i} + \frac{\partial}{\partial x_i}\Big(E_{vs}(v_{si} + u_i)\Big), \qquad (2.11)$$

where $E_{vs} = \sum_\alpha n_{s_\alpha}\epsilon_{s_\alpha}$ is the vibrational energy per unit volume, and $q_{vsi} = \sum_\alpha n_{s_\alpha}\epsilon_{s_\alpha} u_{s_{\alpha_i}}$ is the vibrational heat flux in the x_i direction. If the external forces $F_{s_{\alpha_i}}$ are independent of the velocity, then the force term in (2.10) is identically zero as it assumed that the distribution function f_{s_α} vanishes at infinity. The source term on the right hand side of (2.10) represents the rate of change of the number of molecules in level α in species s. This can be written as

$$\sum_\alpha \int_{-\infty}^{\infty} \epsilon_{s_\alpha} (C_{s_\alpha}^+ - C_{s_\alpha}^-)\, dv_{s_\alpha} = \sum_\alpha \epsilon_{s_\alpha} \left(\frac{\partial n_{s_\alpha}}{\partial t}\right)_{coll}. \qquad (2.12)$$

Combining the above expressions we have

$$\frac{\partial E_{vs}}{\partial t} + \frac{\partial}{\partial x_i}\Big(E_{vs} u_i + E_{vs} v_{si} + q_{vsi}\Big) = \sum_\alpha \epsilon_{s_\alpha} \left(\frac{\partial n_{s_\alpha}}{\partial t}\right)_{coll} = Q_{Vib}. \qquad (2.13)$$

To find an expression for Q_{Vib} we formally need to make the following assumptions:

1. The system of interest is a dilute mixture of vibrating-dissociating molecules and atoms weakly interacting with an infinite heat bath.

2. The Born-Oppenheimer approximation holds so that the vibrational states are uncoupled from the rotational and electronic states of the molecule.

3. The interaction Hamiltonian which causes transition between vibrational levels can be treated as a perturbation on the energy of the vibrating molecules. Thus, quantum mechanical perturbation theory can be used to derive the master relaxation equation.

Under these assumptions Heims (Ref. 30) showed

$$\frac{\partial n_{s_\alpha}}{\partial t} = \nu_{s_\alpha} \left(N_s - 2\,n_s\right)^2 - \mu_{s_\alpha}\, n_{s_\alpha} + \sum_i \left(a_{s_{i\alpha}} n_{s_i} - a_{s_{\alpha i}} n_{s_\alpha}\right), \qquad (2.14)$$

where N_s is the number of s atoms, n_s is the number molecules of species s, $a_{s_{lk}}$ is the transition probability per unit time from vibrational level l to k, ν_{s_α} is the recombination rate of atoms to molecules in level α, and μ_{s_α} is the dissociation rate from level α.

Evaluating the source term Q_{Vib} yields

$$Q_{Vib} = \sum_\alpha \epsilon_{s_\alpha} \left[\nu_{s_\alpha} \left(N_s - 2\,n_s\right)^2 - \mu_{s_\alpha}\, n_{s_\alpha} + \sum_i \left(a_{s_{i\alpha}}\, n_{s_i} - a_{s_{\alpha i}}\, n_{s_\alpha}\right)\right], \qquad (2.15)$$

The first two terms of (2.15) are respectively the gain and loss of vibrational energy due to chemical reactions. The last two terms of (2.15) account for the exchange of vibrational and translational energy due to collisions. At the microscopic level, these two processes are not linked and can be treated independently. Thus we define

$$Q_{Chem} = \sum_\alpha \epsilon_{s_\alpha} \left(\nu_{s_\alpha} \left(N_s - 2\,n_s\right)^2 - \mu_{s_\alpha}\, n_{s_\alpha}\right) \qquad (2.16)$$

and

$$Q_{V-T} = \sum_\alpha \epsilon_{s_\alpha} \sum_i \left(a_{s_{i\alpha}}\, n_{s_i} - a_{s_{\alpha i}}\, n_{s_\alpha}\right). \qquad (2.17)$$

To find an expression for Q_{Chem} we sum (2.14) over all α levels and define

$$\gamma_s = \sum_\alpha \nu_{s_\alpha}, \qquad \mu_s = \sum_\alpha \frac{\mu_{s_\alpha}\, n_{s_\alpha}}{n_s}, \qquad (2.18)$$

where γ_s is the recombination rate and μ_s is the dissociation rate of s molecules. This gives

$$\left(\frac{\partial n_s}{\partial t}\right)_{coll} = \gamma_s \left(N_s - 2\,n_s\right)^2 - \mu_s\, n_s, \qquad (2.19)$$

where $\gamma_s \left(N_s - 2n_s\right)^2$ and $n_s\,\mu_s$ represent the rate of change of the number of molecules of species s per unit time and unit volume due to the forward and backward chemical reactions, respectively. In (2.2), let $w_s = w_{f_s} + w_{b_s}$ so that w_{f_s} and w_{b_s} are the rates of change of the mass of species s per unit time and unit volume due to the forward and backward chemical reactions, respectively. This implies

$$\gamma_s \left(N_s - 2n_s\right)^2 = \frac{w_{b_s}}{m_s} \qquad n_s\,\mu_s = -\frac{w_{f_s}}{m_s}. \qquad (2.20)$$

The average vibrational energy gained during recombination and the average vibrational energy lost during dissociation are the weighted averages of the level-specific dissociation rates multiplied by the vibrational energy of each level. They are respectively:

$$
\begin{aligned}
\overline{G} &= \frac{\sum_\alpha \epsilon_{s_\alpha} \nu_{s_\alpha}}{\sum_\alpha \nu_{s_\alpha}} = \frac{\sum_\alpha \epsilon_{s_\alpha} \nu_{s_\alpha}}{\gamma_s} \\
\overline{E} &= \frac{\sum_\alpha \mu_{s_\alpha} n_{s_\alpha} \epsilon_{s_\alpha}}{\sum_\alpha \mu_{s_\alpha} n_{s_\alpha}} = \frac{\sum_\alpha \mu_{s_\alpha} n_{s_\alpha} \epsilon_{s_\alpha}}{n_s \, \mu_s}.
\end{aligned}
\tag{2.21}
$$

In general, the n_{s_α} in the above equations are functions of T and T_v. However at equilibrium $T = T_v$, and we can define $n_{s_\alpha}^*$ as the number density at equilibrium. Thus we have

$$
\nu_{s_\alpha} (N_s - 2 \, n_s^*)^2 - \mu_{s_\alpha} \, n_{s_\alpha}^* + \sum_i \left(a_{s_{i\alpha}} \, n_{s_i}^* - a_{s_{\alpha i}} \, n_{s_\alpha}^* \right) = 0.
\tag{2.22}
$$

Now we make the assumption that at equilibrium each process must be in equilibrium independent of the other process. This is consistent with the fact that we are treating Q_{Chem} and Q_{V-T} as independent on a microscopic level. This gives

$$
\nu_{s_\alpha} (N_s - 2 \, n_s^*)^2 - \mu_{s_\alpha} \, n_{s_\alpha}^* = 0.
\tag{2.23}
$$

If the transition probabilities are independent of time, (2.22) must hold for all time. If we substitute the expressions for ν_{s_α} from the above equation into (2.16), after some manipulation we find

$$
\overline{E} = \frac{\sum_\alpha \mu_{s_\alpha} n_{s_\alpha}^* \epsilon_{s_\alpha}}{\sum_\alpha \mu_{s_\alpha} n_{s_\alpha}^*}.
\tag{2.24}
$$

If we write $\overline{E} = \overline{E}(T, T_v)$, we immediately see that $\overline{G} = \overline{E}(T, T)$.

Therefore, any physically consistent model for the vibrational energy source term due to chemical reactions must be of the form

$$
Q_{Chem} = \frac{1}{m_s} \left(\overline{E}(T, T_v) \, w_{f_s} + \overline{E}(T, T) \, w_{b_s} \right).
\tag{2.25}
$$

An expression for Q_{V-T} was originally derived by Landau and Teller (Ref. 40) for simple harmonic oscillators not undergoing dissociation. They found

$$
Q_{V-T} = \frac{E_{v_s}(T) - E_{v_s}(T_v)}{\tau_{vib}},
\tag{2.26}
$$

where τ_{vib} is the vibrational relaxation time, and is given by a theoretically determined expression as a function of the local thermodynamic state of the gas. Under more general

conditions, Q_{V-T} will have the above form, but τ_{vib} will be different and will also depend on the oscillator model used.

The equation for the conservation of vibrational energy of species s has the final form:

$$\frac{\partial E_{vs}}{\partial t} + \frac{\partial}{\partial x_i}\big(E_{vs}\, u_i + E_{vs}\, v_{si} + q_{vsi}\big) = Q_{V-T} + Q_{Chem}. \tag{2.27}$$

For the case where there is more than one vibrationally excited species, an additional term must be included to account for the rate of vibrational energy transfer to species s from the other vibrationally excited species (Ref. 68).

If the vibrational energy modes are tightly coupled, then there will be a single vibrational temperature T_v, and the total vibrational energy equation is:

$$\frac{\partial E_v}{\partial t} + \frac{\partial}{\partial x_i}\Big(E_v\, u_i + \sum_s E_{vs} v_{si} + \sum_s q_{vsi}\Big) = \sum_s Q_{V-Ts} + \sum_s Q_{Chems}. \tag{2.28}$$

where $E_v = \sum_s E_{vs}$. Recent work using the results of computational chemistry and quasi-classical trajectory analysis has shed additional light on the magnitude of the energy removal and disposal terms. See Ref. 13 for details.

2.2.5 Additional Internal Energy Conservation Equations

In a similar fashion, conservation expressions for the other internal energy modes (rotational and electronic) may be derived. In practice, unless the conditions of interest are at very low density, the rotational and translational energies are usually considered to be in equilibrium. This obviates the need for a separate rotational conservation equation. Also, if there is appreciable population of the excited electronic states, it is often assumed that the temperatures that characterize the free electron translational energy and the bound excited electronic energy are the same. That leads to a single electron-electronic energy conservation equation. In many cases, it is valid to assume that the vibrational modes are also in equilibrium with the electron-electronic energy (because of resonant coupling between the N_2 vibration and free electrons (Refs. 42, 68)). Then, the vibrational energy equation (2.13) is extended to include these effects.

There is uncertainty about how to model the energy in the free electron and electronic energy modes. We favor the approach of Gnoffo et $al.$ (Ref. 21) in which it is assumed that $T_v = T_e = T_{e\ell}$. Namely, that because of the strong electron-vibration coupling in high temperature air, we typically have $T_v = T_e$. It is probably reasonable to assume that $T_e = T_{e\ell}$. (There really is no other alternative, in any case.) The other approach is to assume that $T = T_e = T_{e\ell}$.

2.3 Electric Field

An expression for the electric field $\tilde{E}_i$ may be derived using the electron momentum conservation equation:

$$\frac{\partial}{\partial t}\left(\rho_e u_i\right) + \frac{\partial}{\partial x_j}\left(\rho_e u_i u_j + p_e \delta_{ij}\right) = -eN_e \tilde{E}_i + P_{ei}, \tag{2.29}$$

where we have neglected the mass diffusion and shear stress terms. P_{ei} represents the momentum transfer between the electrons and the heavy particles due to collisions. For weakly ionized flows, this term is small relative to the electric field term. Then, if we take the ratio of the dynamic pressure of the electron gas to the electron pressure and assume that the electron speed and temperature are about the same as the bulk gas, we have

$$\frac{\rho_e V_e^2}{p_e} = \frac{M_e V_e^2}{RT_e} \simeq \frac{M_e V^2}{RT} \simeq \frac{M_e}{M}\mathcal{M}^2. \tag{2.30}$$

Where $\mathcal{M}$ is the Mach number, and M is the average molecular weight of the mixture. The ratio M_e/M is of the order of 10^{-6}, and for conditions of interest the square of the Mach number will be of the order of 10^3 at most. Therefore, we can neglect the electron dynamic pressure relative to the electron pressure, and the steady-state electric field may be expressed as

$$\tilde{E}_i \simeq -\frac{1}{N_e e}\frac{\partial p_e}{\partial x_i}. \tag{2.31}$$

This expression for the electric field may be inserted in the momentum equation, (2.5), and the total energy equation, (2.7). Generally, this term has little effect on the flow field of atmospheric entry vehicles and is often neglected.

2.4 Equations of State

The relationship between the conserved quantities and the non-conserved quantities such as pressure and temperature are discussed in this section. The total energy, E, is made up of the separate components of energy:

$$E = \sum_{s \neq e}^{ns} E_{ts} + \sum_{s \neq e}^{ns} E_{rs} + \sum_{s \neq e}^{ns} E_{vs} + E_e + \sum_{s \neq e}^{ns} E_{el\,s} + \tfrac{1}{2}\rho u_i u_i + \sum_{s \neq e}^{n} \rho_s h_s^{\circ}, \qquad (2.32)$$

which are the translational, rotational, vibrational, electron translational, electronic, kinetic, and chemical energies, respectively. The heavy particle translational energy is $E_{ts} = \rho_s c_{vts} T$, where $c_{vst} = \tfrac{3}{2} R/M_s$ and T is the translational temperature. The rotational energy is $E_{rs} = \rho_s c_{vrs} T_r$, and $c_{vrs} = R/M_s$ if the particle has two degrees of rotational freedom; T_r is the rotational temperature. As discussed above, for the case where the rotational energy modes relax quickly, we can assume that the rotational energy modes are equilibrated with the translational energy modes. Then, we can write $E_{ts} + E_{rs} = \rho_s c_{vs} T$, where c_{vs} and T are the translational-rotational specific heat and temperature, respectively.

The vibrational temperature of species s is determined by inverting the expression for the vibrational energy contained in a simple harmonic oscillator at the temperature T_{vs}:

$$E_{v_s} = \rho_s e_{vs} = \rho_s \frac{R}{M_s} \frac{\theta_{vs}}{e^{\theta_{vs}/T_{vs}} - 1}, \qquad (2.33)$$

where θ_{vs} is the characteristic temperature of vibration. If we assume that there is a single vibrational temperature, we must invert a more complicated expression for T_v

$$E_v = \sum_s \rho_s \frac{R}{M_s} \frac{\theta_{vs}}{e^{\theta_{vs}/T_v} - 1}. \qquad (2.34)$$

The free electron translational energy is given by $E_e = \rho_e c_{ve} T_e$, where $c_{ve} = \tfrac{3}{2} R/M_e$. In cases where the electron energy is assumed to be in equilibrium with another energy mode, a different temperature is used in the above expression.

As discussed above, the total pressure is the sum of the partial pressures,

$$p = \sum_{s \neq e}^{ns} \rho_s \frac{R}{M_s} T + p_e, \qquad (2.35)$$

and the electron pressure is given by

$$p_e = \rho_e \frac{R}{M_e} T_e. \qquad (2.36)$$

19

The enthalpy per unit mass, h_s, is defined to be

$$h_s = c_{vts}T + c_{vrs}T_r + e_{vs} + e_{el\,s} + h_s^\circ + \frac{p_s}{\rho_s}. \tag{2.37}$$

The expression for the energy contained in the excited electron states comes from the assumption that they are populated according to a Boltzmann distribution governed by the electronic temperature, T_{el}. This yields

$$e_{el\,s} = \frac{R}{M_s}\frac{\sum_{i=1}^{\infty} g_{is}\theta_{el\,is}\exp(-\theta_{el\,is}/T_{el})}{\sum_{i=0}^{\infty} g_{is}\exp(-\theta_{el\,is}/T_{el})}, \tag{2.38}$$

where g_{is} is the degeneracy of the excited electronic state i and $\theta_{el\,is}$ is the excitation energy of that state (Ref. 68). Usually only the first several terms in these summations are required for hypersonic applications.

Another approach is to use the fits for pure species thermodynamics data from Gordon and McBride (Ref. 23). With this approach, the species translational-rotational energy and chemical energy can be subtracted from the total species energy to obtain the vibrational-electronic energy. These curve-fits are valid to high temperature $(20,000\,\mathrm{K})$ and result in a more accurate characterization of the internal energy.

2.5 Diffusion Velocity, Shear Stress, and Heat Flux

The shear stresses are assumed to be proportional to the first derivative of the mass-averaged velocities, and the Stokes assumption for the bulk viscosity is made.[3]

Therefore the expression for the shear stress tensor is

$$\tau_{ij} = \mu\Big(\frac{\partial u_i}{\partial x_j} + \frac{\partial u_j}{\partial x_i}\Big) + \lambda\frac{\partial u_k}{\partial x_k}\delta_{ij}, \qquad \lambda = -\frac{2}{3}\mu. \tag{2.39}$$

And the heat conduction vectors are assumed to be given by the Fourier heat law

$$q_{trj} = -\kappa\frac{\partial T}{\partial x_j}, \qquad q_{vsj} = -\kappa_{vs}\frac{\partial T_{vs}}{\partial x_j}. \tag{2.40}$$

---

[3] The subject of bulk viscosity is interesting. It has long been recognized that the internal energy modes of a gas may affect the speed of sound (Refs. 10, 26, 40, 75). This is commonly attributed to the bulk viscosity because sound propagation is a dilatational process, and the bulk viscosity provides a means of changing the speed of sound due to non-zero dilatation. However, this is not physically consistent. Instead, the proper finite-rate internal energy relaxation equations should be used to obtain the correct speed of sound.

In some cases, it is preferable to represent the vibrational energy conduction with the gradient of the specific vibrational energy.

$$q_{vsj} = -\tilde{\kappa}_{vs}\frac{\partial e_{vs}}{\partial x_j}. \tag{2.41}$$

Except at very high enthalpy, we find that the vibrational energy gradients give more robust results.

A viscosity model for reacting air developed by Blottner *et al* (Ref. 3) may be used to determine the species viscosity, μ_s. This work uses kinetic theory to find curve-fit expressions for the viscosity of each species. Another source of expressions for nonequilibrium calculations may be found in the work of Gupta *et al.* (Ref. 28). This information is too extensive to include in these notes. Excellent reviews of the calculation of species transport properties are given by Palmer and Wright (Refs. 61, 62; see also Refs. 44, 87-89).

The approximate conductivity of the translational-rotational and vibrational temperatures for each species may be derived from an Eucken relation (Ref. 83). With this approach, it is assumed that the transport of translational energy involves correlation with the velocity, but the transport of internal energy (rotational and vibrational) has no correlation. The result is that

$$\kappa_s = \mu_s\left(\frac{5}{2}c_{vts} + c_{vrs}\right), \qquad \kappa_{vs} = \eta_v\mu_s c_{vvs}, \tag{2.42}$$

where $\eta_v = 1.2$ is derived from kinetic theory (Ref. 60), and c_{vvs} is the species s vibrational specific heat. When vibrational energy derivatives are used, the transport coefficient becomes:

$$\tilde{\kappa}_{vs} = \eta_v\mu_s. \tag{2.43}$$

This approach based on the Eucken relation is approximate and is only valid up to about 6000 K for air; at higher temperatures a more sophisticated approach must be used. Palmer and Wright (Refs. 61, 62) provide a quantitative assessment of the available approaches.

Once the pure species viscosity and conductivity have been computed, the mixture properties must be obtained. This is often done with the Wilke semi-empirical mixing rule (Ref. 84), however Palmer and Wright show that this approach is subject to serious error. They recommend the use of the Armaly-Sutton (Ref. 1) mixing rule because it is more accurate and less costly than the solution of the full multi-component diffusion equations. However, the parameters in the Armaly-Sutton model may need to be tuned for particular gas mixtures and conditions (Refs. 61, 62).

If we assume that the diffusive fluxes due to pressure and temperature gradients are negligible, then the diffusion velocity of each component of the gas mixture is proportional to the gradient of the mass fraction. With the additional assumption of binary diffusion where species s diffuses into a mixture of similar particles, we have

$$\rho_s v_{sj} = -\rho D_s \frac{\partial c_s}{\partial x_j}. \tag{2.44}$$

The diffusion coefficient, D_s, is derived by assuming a constant Lewis number, Le, which by definition is given by

$$Le = \frac{\rho \, D c_p}{\kappa}. \tag{2.45}$$

For air, Le is typically taken to have a value of 1.4, and thus the uncharged particles all have the same D, but the diffusion coefficient for ions is assumed to be doubled (the ambipolar diffusion assumption holds) because of the existence of an electric field.

A much more accurate approach for computing diffusion in a gas mixture is the self-consistent effective binary diffusion (SCEBD) approach of Ramshaw and Chang (Refs. 72, 73) and the extension of the method to multi-temperature plasmas (Ref. 74). This approach has been shown to yield accurate results for high-enthalpy atmospheric entry flows (Ref. 24). At atmospheric entry conditions (particularly when the gas is ionized), the constant Lewis number approximation is not valid, and the SCEBD approach should be used.

2.6 Internal Energy Relaxation Rates

The rate of energy exchange between vibrational and translational modes has been discussed extensively (Ref. 40). The rate of change in the population of the vibrational states at low temperatures is described well by the Landau-Teller formulation where it is assumed that the vibrational level of a molecule can change by only one quantum level at a time. The resulting energy exchange rate is

$$Q_{V-Ts} = \rho_s \frac{e_{vs}^*(T) - e_{vs}}{<\tau_{s_{L-T}}>}. \tag{2.46}$$

Where $e_{vs}^*(T)$ is the vibrational energy per unit mass of species s evaluated at the local translational temperature and $<\tau_{s_{L-T}}>$ is the molar averaged Landau-Teller relaxation time

$$<\tau_{s_{L-T}}> = \frac{\sum_r X_r}{\sum_r X_r / \tau_{sr_{L-T}}}, \quad \text{for } r \neq e. \tag{2.47}$$

An expression developed by Millikan and White (Ref. 57) yields the Landau-Teller inter-species relaxation times, $\tau_{sr_{\text{L-T}}}$, in seconds using the function

$$
\begin{aligned}
\tau_{sr_{\text{L-T}}} &= \frac{1}{p} \exp\left[A_{sr}(T^{-1/3} - 0.015\mu_{sr}^{1/4}) - 18.42\right], \quad p \text{ in atm,} \\
A_{sr} &= 1.16 \times 10^{-3}\mu_{sr}^{1/2}\theta_{vs}^{4/3}, \\
\mu_{sr} &= M_s M_r/(M_s + M_r).
\end{aligned}
\tag{2.48}
$$

There are notable exceptions to the Millikan-White formula, particularly for N_2 and O_2 vibration-translation relaxation involving atomic oxygen, and the relaxation of CO_2 (Ref. 68).

A modification to the translational-vibrational relaxation rate is made to account for the limiting collision cross-section at high temperatures. The Landau-Teller rate expression from Millikan and White yields a relaxation rate that is unrealistically large at high temperatures due to an overprediction of the collision cross-section. The addition of the limiting cross-section rate corrects this inaccuracy. As suggested by Park (Ref. 68), a new relaxation time, τ_{vs}, that is the sum of the Landau-Teller relaxation time and the collision-limited relaxation time, τ_{cs}, corrects this inadequacy. Thus if we use (2.46) with this new rate, we have the final form of the translational-vibrational energy exchange rate:

$$
\begin{aligned}
Q_{V-T_s} &= \rho_s \frac{e_{vs}^*(T) - e_{vs}}{\tau_{vs}}, \\
\tau_{vs} &= <\tau_{s_{\text{L-T}}}> + \tau_{cs},
\end{aligned}
\tag{2.47}
$$

where

$$
\tau_{cs} = \frac{1}{\bar{c}_s \sigma_v N_s}.
\tag{2.49}
$$

$\bar{c}_s$ is the average molecular speed of species s, $\bar{c}_s = \sqrt{8RT/\pi M_s}$, and N_s is the number density of the colliding particles. The expression for the limiting collision cross-section, σ_v, is assumed to be as given by Ref. 68:

$$
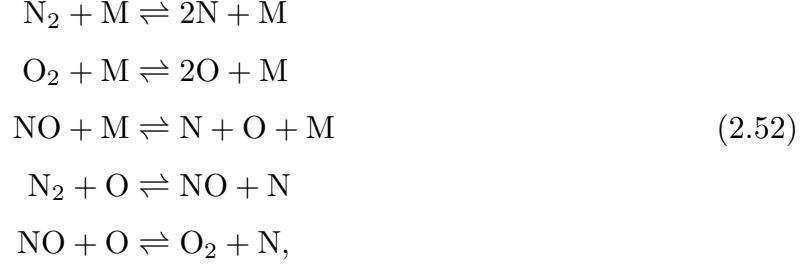\sigma_v = 10^{-17}(50,000/T)^2 \quad \text{cm}^2,
\tag{2.51}
$$

where T is in K. This expression was originally developed for nitrogen, but has been applied to the other diatomic molecules.

2.7 Chemical Source Terms

The source term for each chemical species may be constructed using the law of mass action (Ref. 83) and a given set of chemical reactions. In this section, we develop the

chemical source terms for a simple chemical kinetics model; it is easy to generalize this discussion to other models.

For high temperature non-ionized air there are five primary components, which may be ordered as follows, N_2, O_2, NO, N, and O. The most important chemical reactions between these species are

$$N_2 + M \rightleftharpoons 2N + M$$

$$O_2 + M \rightleftharpoons 2O + M$$

$$NO + M \rightleftharpoons N + O + M \qquad (2.52)$$

$$N_2 + O \rightleftharpoons NO + N$$

$$NO + O \rightleftharpoons O_2 + N,$$

where M represents any particle that acts as a collision partner in the reaction. The first three are dissociation reactions and the remaining two are exchange reactions. Each reaction is governed by forward and backward reaction rate coefficients, k_{f_m} and k_{b_m}, respectively. These five reactions may be written in order in terms of the reaction rates as

$$\mathcal{R}_1 = \sum_m \left[-k_{f_{1m}} \frac{\rho_{N_2}}{M_{N_2}} \frac{\rho_m}{M_m} + k_{b_{1m}} \frac{\rho_N}{M_N} \frac{\rho_N}{M_N} \frac{\rho_m}{M_m} \right]$$

$$\mathcal{R}_2 = \sum_m \left[-k_{f_{2m}} \frac{\rho_{O_2}}{M_{O_2}} \frac{\rho_m}{M_m} + k_{b_{2m}} \frac{\rho_O}{M_O} \frac{\rho_O}{M_O} \frac{\rho_m}{M_m} \right]$$

$$\mathcal{R}_3 = \sum_m \left[-k_{f_{3m}} \frac{\rho_{NO}}{M_{NO}} \frac{\rho_m}{M_m} + k_{b_{3m}} \frac{\rho_N}{M_N} \frac{\rho_O}{M_O} \frac{\rho_m}{M_m} \right] \qquad (2.53)$$

$$\mathcal{R}_4 = -k_{f_4} \frac{\rho_{N_2}}{M_{N_2}} \frac{\rho_O}{M_O} + k_{b_4} \frac{\rho_{NO}}{M_{NO}} \frac{\rho_N}{M_N}$$

$$\mathcal{R}_5 = -k_{f_5} \frac{\rho_{NO}}{M_{NO}} \frac{\rho_O}{M_O} + k_{b_5} \frac{\rho_{O_2}}{M_{O_2}} \frac{\rho_N}{M_N}.$$

Thus, the source terms that represent the inter-species mass transfer rates may be constructed as

$$w_{N_2} = M_{N_2}(\mathcal{R}_1 + \mathcal{R}_4)$$

$$w_{O_2} = M_{O_2}(\mathcal{R}_2 - \mathcal{R}_5)$$

$$w_{NO} = M_{NO}(\mathcal{R}_3 - \mathcal{R}_4 + \mathcal{R}_5) \qquad (2.54)$$

$$w_N = M_N(-2\mathcal{R}_1 - \mathcal{R}_3 - \mathcal{R}_4 - \mathcal{R}_5)$$

$$w_O = M_O(-2\mathcal{R}_2 - \mathcal{R}_3 + \mathcal{R}_4 + \mathcal{R}_5).$$

We should note that the sum of the mass transfer rates is identically zero and that elemental conservation holds, as required.

In equilibrium, the forward and backward reaction rates of reaction m have the functional form:

$$k_{f_m}(T) = C_{f_m} T^{\eta_m} \exp(-\theta_m/T),$$
$$k_{b_m}(T) = \frac{k_{f_m}(T)}{K_{\mathrm{eq}_m}(T)}, \qquad (2.55)$$

where the constants C_{f_m}, η_m, and θ_m are experimentally determined (*e.g.* Refs. 69, 70) or computed using computational chemistry, and K_{eq_m} is computed from first principles using thermodynamic data (Ref. 23). However as discussed by many authors and as shown in Sec. 2.2.4, the vibrational state of the gas affects the dissociation rate. Many models for the vibration-dissociation coupling process have been proposed. We will discuss the most widely used of these models here.

The most widely used, because of its simplicity, is the Park TT_v model, in which the temperature that governs the forward reaction rate is replaced by an effective or average temperature, T_a. Park originally proposed that $T_a = \sqrt{TT_v}$, however a more appropriate expression is

$$T_a = T^\phi T_v^{1-\phi}, \qquad (2.56)$$

where ϕ is usually taken as 0.7. This model is based on some more-or-less heuristic reasoning, but it seems to work well and gives reasonable results. However as we saw during the derivation of the vibrational energy conservation equation, the chemical reaction rate implies a certain rate of vibrational energy removal due to the reactions. This energy removal rate is state-specific, so unless the reaction rate model is state specific, it is impossible to derive an appropriate Q_{Chem} (see (2.25)). Typically, it is assumed that $Q_{Chem} = 0.3D_e$, where D_e is the dissociation energy.

Other authors have used a more detailed derivation of the vibration-dissociation coupling process. For example, the CVDV (coupled vibration-dissociation-vibration) model of Marrone and Treanor (Refs. 55, 81) assumes a Boltzmann distribution of the vibrational states, and allows preferential removal due to dissociation from the upper states. This results in an effective dissociation rate that is a function of the vibrational and translational temperatures and the parameter U:

$$k_f = \frac{Q(T)\,Q(T_F)}{Q(T_v)\,Q(-U)}\,C_f\,T^\eta\,e^{-\theta/T}, \qquad (2.57)$$

where $Q(T)$ is the vibrational partition function evaluated at temperature T and is defined as

$$Q(T) = \sum_{\alpha=0}^{N} e^{-\epsilon_\alpha/kT}. \qquad (2.58)$$

In (2.57) T_F represents a modified temperature and is given by

$$\frac{1}{T_F} = \frac{1}{T_v} - \frac{1}{T} - \frac{1}{U}. \tag{2.59}$$

For $U = \infty$ there is an equal probability of dissociation from all levels, and as U decreases, the probability increases that a dissociating molecule comes from an upper vibrational energy level. $U = 1/3$ is typically used.

The CVDV model naturally results in an expression for Q_{Chem}. The expressions for the energy removed and gained during reactions found in (2.25) are:

$$\begin{aligned}
\overline{E}(T,T_v) &= \frac{1}{Q(T_F)} \sum_{\alpha=0}^{N} \epsilon_\alpha \, e^{-\epsilon_\alpha/kT_F}, \\
\overline{E}(T,T) &= \frac{1}{Q(-U)} \sum_{\alpha=0}^{N} \epsilon_\alpha \, e^{\epsilon_\alpha/kU}.
\end{aligned} \tag{2.60}$$

Knab, Frühauf $et\ al.$ (Refs. 36-38) developed the CVCV (coupled vibration-chemistry-vibration) model that generalizes the approach of Marrone and Treanor. This leads to expressions for the effective reaction rate and the vibrational energy loss terms that are similar to the CVDV results.

The Macheret and Rich (Ref. 53) model takes a classical approach to the coupling problem. As opposed to the discrete energy levels of the real oscillator, Macheret and Rich assume that the vibrational energy distribution function can be approximated by

$$\begin{aligned}
f(\epsilon_v) &= \frac{1}{kT_v} e^{-\epsilon_v/kT_v} && \text{if } \epsilon_v \leq \epsilon_1 \\
&= \frac{1}{kT_v} e^{-\frac{\epsilon_1}{kT_v} - \frac{\epsilon_v - \epsilon_1}{kT}} && \text{if } \epsilon_v > \epsilon_1,
\end{aligned} \tag{2.61}$$

where ϵ_1 is approximately one half of the dissociation energy.

This distribution function is an attempt to take into account the fact that the vibrational energy mode does not relax through a series of Boltzmann distributions. Macheret and Rich assume that the nonequilibrium distribution function can be characterized by a Boltzmann distribution at temperature T_v for the lower levels and another Boltzmann distribution at temperature T for the upper levels. The expression for vibrational energy becomes

$$E_v(T_v,T) = \frac{\rho_{\text{N2}}}{m_{\text{N2}}} \frac{\int_0^{De} \epsilon_v \, f(\epsilon_v) \, d\epsilon_v}{\int_0^{De} f(\epsilon_v) \, d\epsilon_v}, \tag{2.62}$$

where D_e is the dissociation energy of the molecule. The vibrational energy is now a weak function of the translational-rotational temperature.

Macheret and Rich generalize the Arrhenius formula for vibrational nonequilibrium by considering a threshold energy function which determines the minimum total energy in a collision necessary for dissociation. The concept of preferential removal is built into this method by the theoretically determined threshold function. This method also accounts for the rotational state of the molecule and can be used for flows with rotational nonequilibrium.

The nonequilibrium dissociation rate is found to be

$$k_f = k_o\big(k_\ell + k_i + k_h\big), \tag{2.63}$$

where k_ℓ, k_i, and k_h are the rates from the low, intermediate, and high vibrational levels. These expressions are complicated and will not be repeated here (Ref. 53). This approach also yields an expression for Q_{Chem} in terms of the parameters of the model and the vibrational and translational temperatures.

There is one critical issue associated with the use of these vibration-dissociation models. It is sometimes difficult to interpret the experimental data used to derive the constants in the Arrhenius expression for the forward reaction rate (2.55). In many cases the reaction rates were measured in shock-heated gas when the gas may be in thermo-chemical nonequilibrium. In this case, it is important to interpret the experimental data in a manner that is consistent with the vibration-dissociation model being used. For example, Park (Refs. 66, 67) made an extensive study of air reaction rates in the light of the TT_v model.

The modeling of vibration-dissociation coupling is still an open issue, and virtually no work has been done in this area in the past 15 years. It may be that with recent results from computational chemistry, it will be possible to study the dissociation process in much greater detail and many of these issues will be resolved.

2.8 Boundary Conditions

The boundary conditions for hypersonic flows can range from very simple (isothermal, non-catalytic surface) to extremely complicated (mass injection with in-depth material response). In this section, we cover only a few of the simpler boundary conditions.

Usually it is appropriate to assume that there is no slip at the body surface, and therefore the velocity on the surface is zero. Often, the wall temperature is either specified due to material properties or the mode of operation of a particular test facility. Seldom

is an adiabatic wall condition used because at hypervelocity conditions this results in unrealistically high surface temperatures. There are several situations that require more complicated surface boundary conditions.

At low densities, there may be velocity and temperature slip at the wall. That is, if the Knudsen layer at the wall has appreciable thickness, the velocity at the vehicle surface may not approach zero. Gökçen (Ref. 22) and others have developed expressions that may be used to calculate the velocity and temperature/energy slip.

When the surface promotes recombination of the gas, a finite-rate wall catalysis model must be used. Typically, the wall catalysis is expressed as a catalytic efficiency of a surface reaction, α_r, in the expression:

$$k_r = \alpha_r \sqrt{\frac{RT_w}{2\pi M_s}}, \tag{2.64}$$

where M_s is the molecular weight of the species that is recombining at the wall, and T_w is the wall temperature. α_r is measured experimentally, and is often a function of temperature. Then, the mass flux of the recombined species at the surface is $\rho_s k_r$. The relevant boundary condition for the surface state can be obtained by equating this mass flux to the diffusive mass flux of the species given by:

$$\dot{m}_s = (\rho D_s)_w \frac{\partial c_s}{\partial n}\bigg|_w = \alpha_r (\rho_s)_w \sqrt{\frac{RT_w}{2\pi M_s}}, \tag{2.65}$$

Using the assumption that the normal-direction pressure gradient is zero and the boundary condition for temperature, the state of the gas on the wall may be computed using an iteration scheme.

In some cases, the vehicle may fly at a free-stream condition for long enough that the surface reaches a locally-constant temperature. When there is no re-radiation from the surface, this is the adiabatic wall condition. However, in cases where there is a high surface temperature, surface re-radiation is important. Then, the convective heat transfer to the surface is balanced by the black-body re-radiation heat transfer rate, $q_{rad} = \sigma \varepsilon T_w^4$.

At very high heating rates, the surface may ablate. Then, the processes of oxidation, sublimation, and spallation must be considered. These processes are complicated and are beyond the scope of these notes.

3. Numerical Methods for Hypersonic Flows

In this section we discuss numerical methods that are appropriate for solving the governing equations discussed above. We will focus on one method, data-parallel line-relaxation (DPLR) (Ref. 86) with modified Steger-Warming flux vector splitting (Ref. 52, 79). This approach has direct connection to other more modern upwind methods, and has been shown to be reliable for a wide range of applications. As we described above, the method used must be parallelizable and implicit so that solutions may be obtained in a reasonable amount of time. See also Ref. 9 for additional details of the numerical approach.

We consider a gas composed of ns species whose translational and rotational modes are in equilibrium. We assume that the vibrational state is characterized by a single vibrational temperature because of strong vibration-vibration coupling. Also, there is no ionization. This gas model can be generalized to include other effects.

3.1 Conservation-Law Form of the Governing Equations

The governing equations for the nonequilibrium flow that were presented in the previous section may be written in a form that is more suitable for the derivation of the numerical method. This is the conservation-law form of the differential equations where the time rate of change of the vector of conserved quantities is balanced by the gradients in the flux vectors and the source vector. In two dimensions the governing equations written in this form are

$$\frac{\partial U}{\partial t} + \frac{\partial F}{\partial x} + \frac{\partial G}{\partial y} = W, \tag{3.1}$$

where the vector of conserved quantities, U, is given by

$$U = \big(\rho_1, \ \rho_2, \ \ldots, \ \rho_{ns}, \ \rho u, \ \rho v, \ E_v, \ E\big)^T. \tag{3.2}$$

The quantities u and v are the mass-averaged velocity components in the x and y directions respectively. The x and y direction fluxes are written as

$$F = \begin{pmatrix} \rho_1(u + u_1) \\ \rho_2(u + u_2) \\ \vdots \\ \rho_{ns}(u + u_{ns}) \\ \rho u^2 + p - \tau_{xx} \\ \rho u v - \tau_{xy} \\ E_v u + \sum_s u_s E_{vs} + q_{vx} \\ (E + p - \tau_{xx})u - \tau_{xy}v + q_{trx} + q_{vx} + \sum_s \rho_s h_s u_s \end{pmatrix} \tag{3.3}$$

$$G = \begin{pmatrix} \rho_1(v + v_1) \\ \rho_2(v + v_2) \\ \vdots \\ \rho_{ns}(v + v_{ns}) \\ \rho u v - \tau_{yx} \\ \rho v^2 + p - \tau_{yy} \\ E_v v + \sum_s v_s E_{vs} + q_{vy} \\ (E + p - \tau_{yy})v - \tau_{yx}u + q_{try} + q_{vy} + \sum_s \rho_s h_s v_s \end{pmatrix} \tag{3.4}$$

where the quantities u_s and v_s are the x and y components of the diffusion velocity of species s. The source vector is made up of terms that represent the mass, momentum, and energy transfer rates, and may be written as:

$$W = \begin{pmatrix} w_1 \\ w_2 \\ \vdots \\ w_{ns} \\ 0 \\ 0 \\ \sum_s Q_{V-Ts} + \sum_s Q_{chems} \\ 0 \end{pmatrix} \tag{3.5}$$

3.2 An Implicit Finite-Volume Method

In two dimensions, the finite-volume approach discretizes the flowfield on a grid of triangular or quadrilateral elements. The x and y locations of the volume corners (nodes) are stored, and the state of the gas is represented with volume-averaged quantities stored at the centroids of the elements. Each face has an outward-pointing surface normal vector, $\vec{S}$, and the volume of each element is given by $\mathcal{V}$. Figure 3.1 gives a graphical representation of this scheme. It is easy to extend this representation to three dimensions.
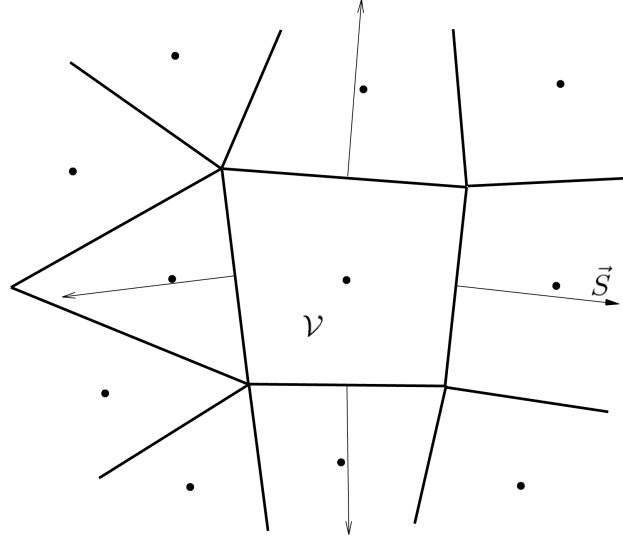
Figure 3.1 – *Numbering scheme for the two-dimensional finite-volume method.*

If we integrate the conservation equations over a finite volume cell, $\mathcal{V}$, we obtain:

$$\frac{\partial}{\partial t} \int_{\mathcal{V}} U \, d\mathcal{V} + \int_{\mathcal{V}} \nabla \cdot \vec{F} \, d\mathcal{V} = \int_{\mathcal{V}} W \, d\mathcal{V} \tag{3.6}$$

$$\frac{\partial \bar{U}}{\partial t} + \frac{1}{\mathcal{V}} \int_{S} \vec{F} \cdot d\vec{S} = \bar{W} \tag{3.7}$$

Where $\vec{F} = F\vec{\imath} + G\vec{\jmath}$, and $\vec{S}$ is the cell surface-normal vector. For a finite volume, we can then interpret this expression as

$$\frac{\partial U}{\partial t} + \frac{1}{\mathcal{V}} \sum_{\text{faces}} \vec{F} \cdot \vec{S} = W, \tag{3.8}$$

where we have dropped the bars, and we sum the fluxes across the faces of the finite volume.

Now, we can obtain a fully implicit method by evaluating the fluxes and the source vector at the future time level, $n + 1$:

$$U^{n+1} - U^n + \frac{\Delta t}{\mathcal{V}} \sum_{\text{faces}} \vec{F}^{n+1} \cdot \vec{S} = \Delta t \, W^{n+1}. \tag{3.9}$$

And then we can linearize the fluxes and source vector as:

$$\begin{aligned}
\vec{F}^{n+1} &\simeq \vec{F}^n + \frac{\partial \vec{F}}{\partial U}\left(U^{n+1} - U^n\right) = \vec{F}^n + \vec{A}^n\left(U^{n+1} - U^n\right) \\
W^{n+1} &\simeq W^n + \frac{\partial W}{\partial U}\left(U^{n+1} - U^n\right) = W^n + C^n\left(U^{n+1} - U^n\right)
\end{aligned} \tag{3.10}$$

Where $\vec{A} = \frac{\partial F}{\partial U}\vec{i} + \frac{\partial G}{\partial U}\vec{j} = A\vec{i} + B\vec{j}$. If we define $\delta U^n = U^{n+1} - U^n$, we obtain the expression:

$$\delta U^n + \frac{\Delta t}{\mathcal{V}} \sum_{\text{faces}} \vec{A}^n \delta U^n \cdot \vec{S} - \Delta t\, C^n \delta U^n = -\frac{\Delta t}{\mathcal{V}} \sum_{\text{faces}} \vec{F}^n \cdot \vec{S} + \Delta t\, W^n \tag{3.11}$$

We need to determine how to evaluate the fluxes at the cell surfaces, given the flow quantities at the cell centroids.

3.2.1 Flux-Vector Splitting

Consider only the inviscid portion of the fluxes; the viscous fluxes are diffusive and it is relatively straight-forward to evaluate them. First, let's derive a simple first-order accurate method developed by Steger and Warming (Ref. 79). For convenience, define a rotated flux vector F' such that

$$F' = F s_x + G s_y \tag{3.12}$$

where s_x and s_y are the direction cosines of the surface normal vector, $\vec{S}$.

We recognize that the inviscid part of F' is homogeneous in U, and therefore $F' = A'U$. We can diagonalize A' and split the eigenvalues into those that are positive and those that are negative:

$$\begin{aligned} F = A'U &= X^{-1}\Lambda_{A'} X\, U \\ &= X^{-1}\Lambda_{A'}^+ X\, U + X^{-1}\Lambda_{A'}^- X\, U \\ &= A'^+ U + A'^- U = F'^+ + F'^- \end{aligned} \tag{3.13}$$

Where $\Lambda_{A'}^+$ is the diagonal matrix of the eigenvalues that are positive, and $\Lambda_{A'}^-$ contains the negative eigenvalues. Physically, F'^+ represents the flux moving in the surface-normal direction, and F'^- is the flux moving in the opposite direction. Therefore, when we evaluate the fluxes at a cell face, we should use information taken from the appropriate location, as seen in Fig. 3.2.
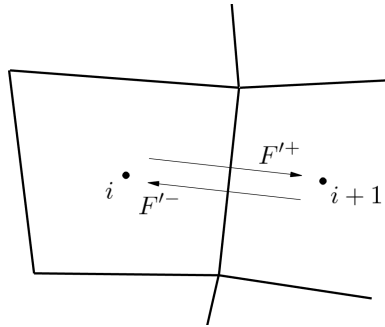

Figure 3.2 – *Illustration of fluxes across a surface.*

Thus, to compute F' at the surface shown above, we use

$$F'_{i+\frac{1}{2},j} = A_i'^+ U_i^n + A_{i+1}'^- U_{i+1}. \tag{3.14}$$

In this expression, Steger and Warming evaluated the Jacobians at the same location as the solution vector; however this leads to a very dissipative method (Ref. 50). Instead, it is much better to average across the face to evaluate the Jacobians using:

$$F'_{i+\frac{1}{2},j} = A_{i+\frac{1}{2}}'^+ U_i^n + A_{i+\frac{1}{2}}'^- U_{i+1}. \tag{3.15}$$

where

$$A_{i+\frac{1}{2}}'^{\pm} = A'^{\pm}\left(\tfrac{1}{2}(U_i + U_{i+1})\right), \tag{3.16}$$

that is, we use the average of the flow quantities on either side of the cell surface to evaluate the Jacobian. This results in much less dissipation than the original Steger-Warming method.

Interestingly, the above approximation for the flux can be written in a different form by combining the flux components:

$$F'_{i+\frac{1}{2}} = F'\left(\tfrac{1}{2}(U_i + U_{i+1})\right) - \frac{1}{2}\left(X^{-1}|\Lambda_{A'}|X\right)(U_{i+1} - U_i) \tag{3.17}$$

where the first term is an unbiased average of the flux at the surface, and the second term is an upwind-biased dissipative flux. This is the familiar Roe form of the flux.

This expression can be used to obtain a first-order accurate approximation to the flux at each face of the element. However, for strong shock waves and other discontinuities, the unbiased averaging across the face will produce aphysical results (negative densities and energies). Therefore, a sensor must be used to smoothly switch back to the more dissipative form of the flux in regions of strong pressure gradient. We use a weight of the form:

$$w = 1 - \frac{1}{2}\frac{1}{(\sigma_g\,\tilde{p})^2 + 1}, \qquad \tilde{p} = \frac{p_i - p_{i+1}}{\min(p_i, p_{i+1})} \tag{3.18}$$

Where w and $1 - w$ are used to weight U_i and U_{i+1} so that the flux is given by (3.14) for $\tilde{p} \to \infty$ and by (3.15) for $\tilde{p} = 0$. The quantity σ_g can be chosen to increase the sensitivity of the sensor to the pressure gradient (a reasonable value for ϵ_g is 5). Crucially, this sensor will not switch on in boundary layers where the pressure gradients are weak.

An additional modification to the flux evaluation method is required for hypersonic flows. In the stagnation region of blunt bodies, the convection speeds are small relative

to the sound speed. In addition, if there is minor misalignment of the grid with the bow shock wave, there can be error generated by the bow shock. This error can become trapped in the stagnation region, resulting in the "carbuncle" phenomenon. In this situation, the error overwhelms the actual flow physics and causes the bow shock to lens upstream in an aphysical manner. There are various ways to prevent the formation of the carbuncle – the best approach is to carefully align the grid with the bow shock wave. However, this is not always possible, and an eigenvalue limiter is commonly applied. Here, the eigenvalues appearing in (3.13) are modified to prevent them from going to zero as Mach number approaches zero. For example, let:

$$\lambda^\pm = \frac{1}{2}\big(\lambda^\pm \pm \sqrt{(\lambda^\pm)^2 + (\epsilon_e a)^2}\big) \tag{3.19}$$

Where ϵ_e is often taken to be about 0.3. This eigenvalue limiter reduces the build-up of error in the stagnation region and helps prevent (but does not always eliminate) the carbuncle from forming. It is important to make $\epsilon_e = 0$ in the wall-normal direction because it can cause artificial diffusion of the boundary layer.

This approximation to the flux is only first-order accurate in space and is essentially worthless for predicting heat transfer rates for hypersonic aerothermodynamics simulations. There are many approaches to obtaining higher-order accuracy for conservation laws. In these notes, we discuss one such approach that has been shown to be effective for a wide range of hypersonic flows. It compares favorably with other popular upwind approaches (Ref. 16), and its form is easy to linearize for use in implicit methods.

The key issue associated with obtaining second-order accuracy is how to accurately project the cell-centered data to the faces without introducing numerical problems. In the approach above, the upwind cell-centroid value of U is taken as the element face value for use in the flux expression. To obtain second-order accuracy, we require a linear fit to U for a more accurate value for $U_{i+\frac{1}{2}}$.

We use the MUSCL approach developed by van Leer (Refs. 82, 90) as our primary approach for approximating U at the element face. A simple upwind extrapolation of the conserved variables to the face on a uniform grid would result in a flux of the form:

$$\begin{aligned}
U^L_{i+\frac{1}{2}} &= \frac{3}{2}U_i - \frac{1}{2}U_{i-1} \\
U^R_{i+\frac{1}{2}} &= \frac{3}{2}U_{i+1} - \frac{1}{2}U_{i+2}
\end{aligned} \tag{3.20}$$

and

$$F'_{i+\frac{1}{2}} = A'^+_{i+\frac{1}{2}}U^L_{i+\frac{1}{2}} + A'^-_{i+\frac{1}{2}}U^R_{i+\frac{1}{2}} \tag{3.21}$$

Where U^L and U^R represent the approximations to $U_{i+\frac{1}{2}}$ using left- and right-biased data. (For simplicity we have assumed a uniformly spaced grid indexed by i.)

This approach yields a formally second-order accurate flux. However, it will cause problems near strong gradient regions because the extrapolation can result in aphysical flow states. Therefore, these gradients must be sensed and the extrapolation reduced or caused to revert to the first-order flux above. With the MUSCL (monotone upwind schemes for conservation laws) approach, the extrapolations are limited to prevent spurious oscillations near large gradients. For example, the extrapolation of each variable in U could be "slope limited." For example, consider limiting the variables ϕ^L and ϕ^R with:

$$
\phi^L_{i+\frac{1}{2}} = \phi_i + \frac{1}{2} \lim \left(\phi_{i+1} - \phi_i, \, \phi_i - \phi_{i-1} \right)
$$
$$
\phi^R_{i+\frac{1}{2}} = \phi_{i+1} - \frac{1}{2} \lim \left(\phi_{i+2} - \phi_{i+1}, \, \phi_{i+1} - \phi_i \right)
$$
(3.22)

where the limiter function can take many forms. We use a minmod limiter that takes the minimum (in magnitude) of the two arguments if they have the same sign; otherwise its value is zero. Note that this approach takes the smaller of the two possible changes to ϕ when the sign of the slopes is the same, and uses no second-order correction when the slopes are of different sign. Such an approach can be shown to be total variation diminishing (TVD) for the linear wave equation.

The most obvious method would be to use the MUSCL approach on each of the conserved variables. Thus, each conserved variable is slope-limited and extrapolated as above. However, we have found that a more robust and accurate second-order extrapolation method can be obtained by applying the MUSCL approach to the primitive variables and then constructing the conserved variables from those quantities. With this approach, we compute $\rho_s^{L,R}, u^{L,R}, v^{L,R}, e_v^{L,R}$, and $p^{L,R}$ using the above expressions and form $U^{L,R}$ from these quantities. This form of second-order fluxes is recommended. It gives more accurate results, and is significantly more robust for large time steps than the simple upwind extrapolation (3.19) or the MUSCL-based conserved variable extrapolation.

A further issue involves how to extrapolate fluxes on non-regular grids. The preceding discussion assumes that the data are available from regularly spaced neighboring elements so that the extrapolations can be performed. However, on a general triangular/quadrilateral grid (tetrahedral/prism/pyramid/hexahedral grid in three dimensions) this is not the case, and there is not a single neighboring element in a sensible upwind direction. In this situation, it is necessary to perform a more sophisticated gradient calculation using a cloud of neighboring points. There are many possible ways to form this

gradient (Ref. 56), but we have found that a weighted least-squares approach gives the most accurate results. Here planes (hyperplanes in three-dimensions) are fitted through a relevant cloud of nearby data points, and the slope of each variable is computed from the slope of the plane. This slope is then used in the MUSCL limiter function shown above. To be specific, consider Figure 3.3 which shows an example for which there is sufficient information to form the gradients with element-centroid data. Thus, the expressions above are used to construct the fluxes for this case. Figure 3.4 shows an example in which three cell-centered values are available to construct the gradients used in the MUSCL slope limiter. In this case, the weighted least-squares approach is used to evaluate the gradient at the left-side element centroid. Then the extrapolated variable in this case is:

$$\phi^L = \phi_i + \nabla\phi_i \cdot d\vec{r} \tag{3.23}$$

where ϕ_i is the variable in the left face neighbor element, $\nabla\phi_i$ is its gradient there, and $\vec{r}$ is the face-to-centroid vector.
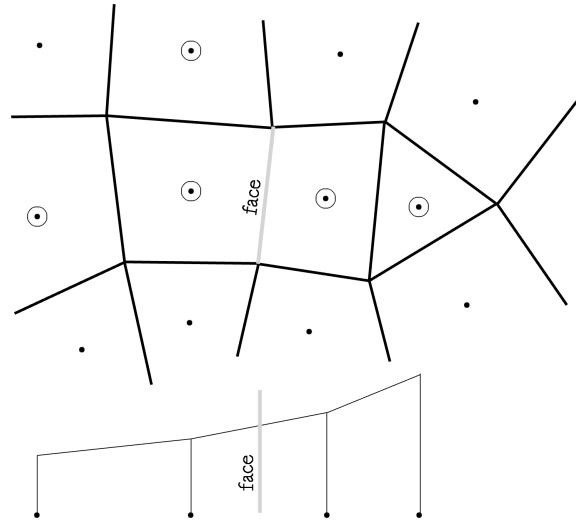
Figure 3.3 – *Example showing how element-centered data are used to construct the flux at the highlighted face.*
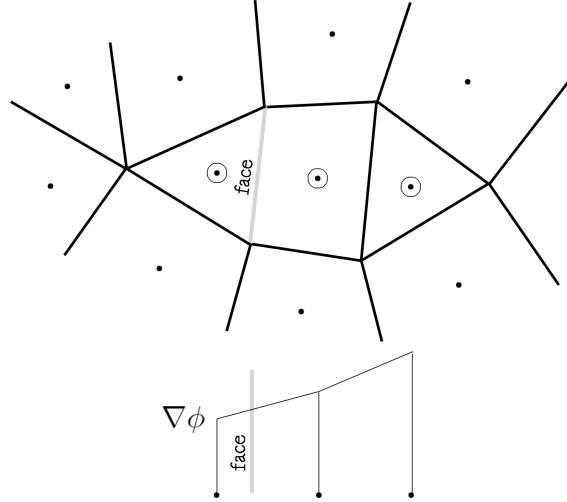
Figure 3.4 – *Example showing how three element-centered values and one weighted least-squares gradient are used to construct the flux at the highlighted face.*

3.2.2 Evaluation of the Diffusive Fluxes

For a structured grid with ordered i, j elements (or i, j, k in three dimensions), it is possible to use grid metrics to evaluate the viscous fluxes. This is straight-forward, and simply involves computing unbiased gradients of the relevant variables. For a general unstructured grid, a different approach must be used. Two approaches are commonly used in the literature: either the Green-Gauss theorem is used to evaluate a gradient by summing around the surface of the element, or a weighted least-squares approach is used. We favor the latter approach, though both are inaccurate in regions of large grid stretching (which is precisely where accurate gradients are required). This problem is particularly severe in regions of high cell-aspect-ratio (CAR), which is the ratio of the longest element side to its shortest side. For this reason, we use a deferred correction approach (Ref. 35) that corrects the gradient estimate using the data nearest to each face.

At an element face, the gradient of some variable ϕ can be written as

$$\nabla\phi = \big(\nabla\phi \cdot \hat{n}\big)\hat{n} + \big(\nabla\phi - \big(\nabla\phi \cdot \hat{n}\big)\hat{n}\big) \tag{3.24}$$

Now, using the terminology illustrated in Fig. 3.5, we can correct the face gradient estimate using the values of $\phi^{L,R}$

$$\widetilde{\nabla\phi} = \frac{\phi^R - \phi^L}{\Delta\ell}(\hat{e} \cdot \hat{n})\hat{n} + \frac{1}{2}\big(I - \hat{n} \otimes \hat{n}\big)\big((\nabla\phi)^L + (\nabla\phi)^R\big) \tag{3.25}$$

where $(\nabla\phi)^{L,R}$ are the weighted-least squares gradient estimates at the left and right cell centers. This approach significantly improves the gradient values in high CAR regions.
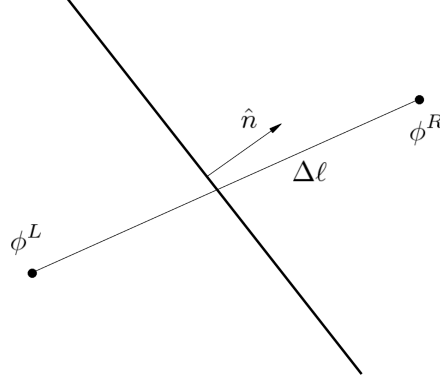
Figure 3.5 – *Deferred correction nomenclature.*

3.2.3 Diagonalization of the Flux Jacobian

Now, let us discuss how to diagonalize the Jacobian matrix, A. (Here we use A for simplicity; the diagonalization of A' follows trivially.) The straight-forward approach would be to form A and then find the eigenvalues and eigenvectors. This is complicated and difficult to do. It is easier to diagonalize A using a different set of variables and then transform back to the conserved variables. A good choice is the vector of "primitive" variables

$$V = \big(\rho_1, \ \rho_2, \ \ldots, \ \rho_{ns}, \ u, \ v, \ e_v, \ p\big)^T, \tag{3.26}$$

where $e_v = E_v/\rho$. Then, we can write

$$A = \frac{\partial F}{\partial U} = \frac{\partial U}{\partial V}\frac{\partial V}{\partial U}\frac{\partial F}{\partial V}\frac{\partial V}{\partial U} \tag{3.27}$$

It turns out that it is easier to diagonalize the matrix $\frac{\partial V}{\partial U}\frac{\partial F}{\partial V}$ than A itself.

We can compute these matrices, but we need some intermediate results, namely derivatives of p with respect to the conserved variables, and derivatives of E with respect to the primitive variables. We can write p in terms of U as:

$$p = \frac{\sum_s \rho_s \frac{R}{M_s}}{\sum_s \rho_s c_{vs}}\Big[E - E_v - \frac{1}{2}\frac{1}{\sum_s \rho_s}\big((\rho u)^2 + (\rho v)^2\big)\Big], \tag{3.28}$$

and therefore,

$$
\begin{aligned}
\frac{\partial p}{\partial \rho_s} &= \Big(\frac{R}{M_s} - \frac{\bar{R}c_{vs}}{c_v}\Big)T + \frac{\bar{R}}{c_v}\Big(\tfrac{1}{2}(u^2 + v^2) - h_s^\circ\Big), \\
\frac{\partial p}{\partial \rho u} &= -u\frac{\bar{R}}{c_v}, \qquad \frac{\partial p}{\partial \rho v} = -v\frac{\bar{R}}{c_v}, \\
\frac{\partial p}{\partial E_v} &= -\frac{\bar{R}}{c_v}, \qquad \frac{\partial p}{\partial E} = \frac{\bar{R}}{c_v}.
\end{aligned}
\tag{3.29}
$$

Where we have defined

$$c_v = \sum_s \frac{\rho_s}{\rho} c_{vs}, \qquad \bar{R} = \sum_s \frac{\rho_s R}{\rho M_s}. \qquad (3.30)$$

The derivatives of E with respect to the non-conserved variables are computed by writing E in terms of these variables as

$$E = \frac{\sum_s \rho_s c_{vs}}{\sum_s \rho_s \frac{R}{M_s}} p + \sum_s \rho_s e_v + \tfrac{1}{2} \sum_s \rho_s (u^2 + v^2) + \sum_s \rho_s h_s^{\circ}. \qquad (3.31)$$

The derivatives that result are

$$\begin{aligned}
\frac{\partial E}{\partial \rho_s} &= \left(c_{vs} - \frac{c_v R}{M_s \bar{R}} \right) T + e_v + \tfrac{1}{2}(u^2 + v^2) + h_s^{\circ}, \\
\frac{\partial E}{\partial u} &= \rho u, \qquad \frac{\partial E}{\partial v} = \rho v, \\
\frac{\partial E}{\partial e_v} &= \rho, \qquad \frac{\partial E}{\partial p} = \frac{c_v}{\bar{R}}.
\end{aligned} \qquad (3.32)$$

The Jacobian matrix, $\frac{\partial V}{\partial U}\frac{\partial F}{\partial V}$, that appears in (3.27) may be constructed from these derivatives:

$$\frac{\partial V}{\partial U}\frac{\partial F}{\partial V} = \begin{pmatrix}
u & 0 & \dots & 0 & \rho_1 & & & \\
0 & u & \dots & 0 & \rho_2 & & & \\
\vdots & \vdots & \ddots & \vdots & \vdots & & & \\
0 & 0 & \dots & u & \rho_{ns} & & & \\
& & & & u & 0 & 0 & 1/\rho \\
& & & & 0 & u & 0 & 0 \\
& & & & 0 & 0 & u & 0 \\
& & & & \rho a^2 & 0 & 0 & u
\end{pmatrix} \qquad (3.33)$$

The speed of sound, a, has been defined such that

$$\rho a^2 = \sum_s \rho_s \frac{\partial p}{\partial \rho_s} + \rho u \frac{\partial p}{\partial \rho u} + \rho v \frac{\partial p}{\partial \rho v} + E_v \frac{\partial p}{\partial E_v} + (E + p) \frac{\partial p}{\partial E}, \qquad (3.34)$$

which may be simplified using the derivatives given above to the expression

$$\begin{aligned}
a^2 &= \left(1 + \frac{\bar{R}}{c_v} \right) \bar{R} T \\
&= \bar{\gamma} \bar{R} T.
\end{aligned} \qquad (3.35)$$

Where we have defined $\bar{\gamma}$ to be the ratio of the frozen translational-rotational specific heats of the gas mixture.

It is straight-forward to diagonalize the Jacobian (3.27). If we write

$$\frac{\partial V}{\partial U}\frac{\partial F}{\partial V} = C_A^{-1}\,\Lambda_A\,C_A, \tag{3.36}$$

the eigenvalues are:

$$\Lambda_A = \mathrm{diag}\left(\underbrace{u,\ u,\ \dots,\ u}_{ns\ \mathrm{elements}},\ u+a,\ u,\ u,\ u-a\right)^T, \tag{3.37}$$

and with this ordering of the eigenvalues, the matrix C_A is

$$C_A = \begin{pmatrix} 1 & 0 & \dots & 0 & \rho_1/a^2 & 0 & 0 & -c_1/a^2 \\ 0 & 1 & \dots & 0 & \rho_2/a^2 & 0 & 0 & -c_2/a^2 \\ \vdots & \vdots & \ddots & \vdots & \vdots & \vdots & \vdots & \vdots \\ 0 & 0 & \dots & 1 & \rho_{ns}/a^2 & 0 & 0 & -c_{ns}/a^2 \\ & & & & \rho a & 0 & 0 & 1 \\ & & & & 0 & 1 & 0 & 0 \\ & & & & 0 & 0 & 1 & 0 \\ & & & & -\rho a & 0 & 0 & 1 \end{pmatrix} \tag{3.38}$$

Where $c_s = \rho_s/\rho$ is the mass fraction of species s.

Note that since the equations that describe the reacting flow have the same features as the perfect gas equations, all of the modern upwind flux evaluation methods may be used. A compact form of the Jacobian can be derived as in Ref. 9.

3.2.4 Jacobian of the Source Vector

To achieve good convergence rates, it is necessary to exactly evaluate the Jacobian of the source vector, $C = \partial W/\partial U$. In my experience, every quantity that appears in W must be differentiated exactly. In many cases, neglecting a seemingly small term can change the sign of some elements of C, making the method converge slowly.

There are many different approaches that may be taken to reduce the difficulty of the algebra. For example, Gökçen (Ref. 22) explicitly expresses W as a function of the temperatures

$$W(U) = \tilde{W}\big(U,\ T(U),\ T_v(U)\big), \tag{3.39}$$

then he computes

$$C = \frac{\partial \tilde{W}}{\partial U} + \frac{\partial \tilde{W}}{\partial T}\frac{\partial T}{\partial U} + \frac{\partial \tilde{W}}{\partial T_v}\frac{\partial T_v}{\partial U}. \tag{3.40}$$

The need for the correct linearization of the source term cannot be understated. Even small algebra or coding errors or simplifications to the linearization can cause severe problems with numerical stability. Thus, this part of the code must be rigorously checked.

3.2.5 Implicit Treatment of the Boundary Conditions

We have not discussed the treatment of the boundary conditions. During the formation of right-hand side of (3.11), the appropriate conditions at the boundaries must be used. For example, at surfaces there must be no slip at the surface, the temperatures must either be given by the isothermal wall condition or set by the adiabatic wall condition, and the normal pressure gradient must be zero or determined from the normal momentum equation. The chemical state of the gas at the wall is found by the catalytic efficiency of the surface.

The implicit treatment of the boundary conditions is just as important, and is less straight-forward. Consider a surface $i + \frac{1}{2}$ such that the element i is used to specify the boundary condition for the flux into element $i + 1$. Then we must express the change in the solution within the boundary cell, δU_i, in terms of the change in the solution within the flow field, δU_{i+1}. This can be done for any boundary condition if we construct a matrix $\mathbf{E}$ such that $\delta U_i = \mathbf{E} \delta U_{i+1}$. Then we can absorb the boundary condition into the block-tridiagonal solution, and we can include the exact boundary conditions in the implicit method, resulting in much improved convergence. For some boundary conditions, it may be difficult or impossible to find an analytic form for $\mathbf{E}$. In that case, $\mathbf{E}$ can be constructed from numerical derivatives of the wall flux.

3.2.6 Implicit Viscous Terms

The evaluation of the viscous fluxes was discussed in section 3.2.2 above. We need to linearize the viscous fluxes, F_v, for use in the implicit method. We can write this flux at the unknown time level as:

$$F_v^{n+1} = F_v^n + \delta F_v^n \tag{3.41}$$

We do not have to have a perfect linearization of F_v, just the largest terms need to be represented. In most flows, there is a direction in which the viscous fluxes dominate. For example, in high Reynolds number flows the viscous terms are large in the boundary layer, and the grid must be stretched close to the surface to resolve the near-wall gradients. In this region the surface-normal viscous fluxes are orders of magnitude larger than the streamwise or spanwise viscous fluxes. Therefore, we need only linearize the normal-direction F_v. This drastically simplifies the problem, and it becomes possible to write δF_v in the form:

$$\delta F_v \simeq M_v \frac{\partial}{\partial n} \big(N_v \delta U \big) \tag{3.42}$$

where n is the wall-normal direction.

In practice, for general unstructured grids it is difficult to identify the wall-normal direction. Rather, we simply linearize the flux due to gradients of the face's nearest-neighbor data.

3.2.7 Data-Parallel Line Relaxation

Let us return to the fully implicit method that we developed above in (3.11):

$$\delta U^n + \frac{\Delta t}{\mathcal{V}} \sum_{\text{sides}} \vec{A}^n \delta U^n \cdot \vec{S} - \Delta t\, C^n \delta U^n = -\frac{\Delta t}{\mathcal{V}} \sum_{\text{sides}} \vec{F}^n \cdot \vec{S} + \Delta t\, W^n$$

Substituting the expressions developed above for $\vec{A}$ and $\vec{F}$, results in a large linear system of equations for δU^n. Because we have used an upwind method, the resulting system of equations is diagonally dominant, making it amenable to solution with iterative methods. There are many such methods in the literature, and each has its pros and cons. Over the past ten years, we have been using the data-parallel line-relaxation (DPLR) method (Ref. 86) for the solution of this system of equations. This method is a parallelizable variant of the Gauss-Seidel line-relaxation method of MacCormack (Ref. 49, 51, 52), and is at the core of the NASA DPLR multi-block structured grid code. This method is designed for use on parallel computers, and is ideally suited to the solution of wall-bounded hypersonic flows. Recently, we have generalized the DPLR method to a certain class of unstructured grids in the US3D code (see also Ref. 85).

The DPLR approach takes (3.11) and recognizes that there is strong physical coupling in the surface-normal direction. If a grid has been generated that has lines of elements running out from the surface (and preferably through the bow shock wave to the free-stream), (3.11) can be modified to reduce its cost of solution. The implicit terms due to the fluxes that are transverse to the wall-normal lines of elements can be moved to the right-hand side and their influence included through a series of sub-iterations. This results in a series of block-tridiagonal solutions, rather than a full matrix solve. This method has the form:

$$\delta U^{(0)} + \frac{\Delta t}{\mathcal{V}} \sum_{\text{on lines}} \vec{A}^n \delta U^{(0)} \cdot \vec{S} - \Delta t\, C^n \delta U^{(0)} = -\frac{\Delta t}{\mathcal{V}} \sum_{\text{sides}} \vec{F}^n \cdot \vec{S} + \Delta t\, W^n$$

Then for $k = 1, k_{max}$

$$\begin{aligned}
\delta U^{(k)} + \frac{\Delta t}{\mathcal{V}} \sum_{\text{on lines}} \vec{A}^n \delta U^{(k)} \cdot \vec{S} - \Delta t\, C^n \delta U^{(k)} = {} & -\frac{\Delta t}{\mathcal{V}} \sum_{\text{sides}} \vec{F}^n \cdot \vec{S} + \Delta t\, W^n \\
& -\frac{\Delta t}{\mathcal{V}} \sum_{\text{off lines}} \vec{A}^n \delta U^{(k-1)} \cdot \vec{S}
\end{aligned} \tag{3.43}$$

And finally:

$$\delta U^n = \delta U^{k_{max}}$$

One detail is that we use only the nearest-neighbor data in the linearization. That is, the terms due to the higher-order variable extrapolation are ignored (for example in (3.21), we would not include the terms due to U_{i-1} and U_{i+2}). This simplifies the linear system, and (as far as we know) does not diminish the convergence rate of the method.

This method can be implemented efficiently in parallel with MPI (message passing interface), and most, if not all, of the communication costs can be hidden through asynchronous communication protocols. Excellent scaling has been obtained on a wide range of parallel computers.

The unstructured grid implementation of this method is the same as above, but requires the construction of surface-normal lines of regular elements. These elements do not have to be regularly connected, but are simply identified as being in a wall-normal line of either hexahedral or prismatic elements. Then the block-tridiagonal solver must be generalized to allow the solution on non-regularly connected lines. This is a straight-forward generalization of standard block-tridiagonal solvers.

4. Examples

4.1 Apollo Command Module Flow

The prediction of hypersonic entry flows is still a challenge for the best numerical methods. There are a number of sources of potential problems, and these include:

- The main quantity of interest is the heat flux, which is a gradient-based quantity and is inherently more difficult to predict than the pressure.

- Many hypersonic entry vehicles have a large stagnation region with high heat fluxes and low convection speeds. Error can get trapped in this region and accumulate, destroying the solution. In some cases, resulting in a so-called "carbuncle."

- The stagnation region is bounded by a very strong shock wave that can inject large error into the flow field.

- The solution is very sensitive to grid resolution and grid alignment with the shock wave. All widely used methods solve the equations of gas dynamics in the grid directions. If the shock wave is not aligned with the grid, the shock will become stair-cased across several cells and large error will be generated.

- Interestingly, solution quality and accuracy may be adversely affected by grid refinement and stretching in the stagnation region.

- The solution is sensitive to the level of dissipation used in the flux evaluation and limiters. Even subtle changes in the flux method can make large differences in the predicted heat fluxes.

In general, great care must be taken in the grid generation, a grid topology with a patch in the stagnation region should be used, and the grid resolution should be as uniform as possible in the stagnation region. The solution quality will increase when the grid is aligned with the bow shock wave. A certain amount of skepticism in the results and patience is required to obtain reliable results for problems at high Mach number and with large stagnation regions.

Consider for example the forebody of a re-entry vehicle similar to the Apollo Command Module. This is a segment of a sphere, with a smaller radius on its edge. (This geometry is a $\pm 20°$ segment of a $10\,\mathrm{m}$ radius sphere, with a $0.5\,\mathrm{m}$ radius cylindrical leading edge added.) Figure 4.1 shows a possible surface grid for this geometry. A two-dimensional grid for one surface-normal slice of the domain has been rotated about the symmetry axis. This results in pie-shaped cells with a singular axis. Such a grid may result in poor solutions

because of the large variation in flow resolution in the subsonic region.

Figure 4.1 also plots the computed surface pressure and heat transfer rate using this grid for the conditions: $\rho_\infty = 8.364 \times 10^{-5}\,\text{kg/m}^3$, $T_\infty = 219.8\,\text{K}$, $v_\infty = 7414\,\text{m/s}$, $\alpha = 19°$, and $T_{wall} = 1500\,\text{K}$. This calculation was performed with the minmod limiter and the variables ρ_s, u, v, w, e_v, and T were extrapolated and limited to obtain second-order accuracy. Note that this is a particularly difficult condition because the angle of attack produces a very large subsonic region where error can accumulate. This grid has 78 points in the radial direction, 61 points in the circumferential direction, and 121 points in the wall normal direction. No attempt has been made to align the grid with the shock wave.
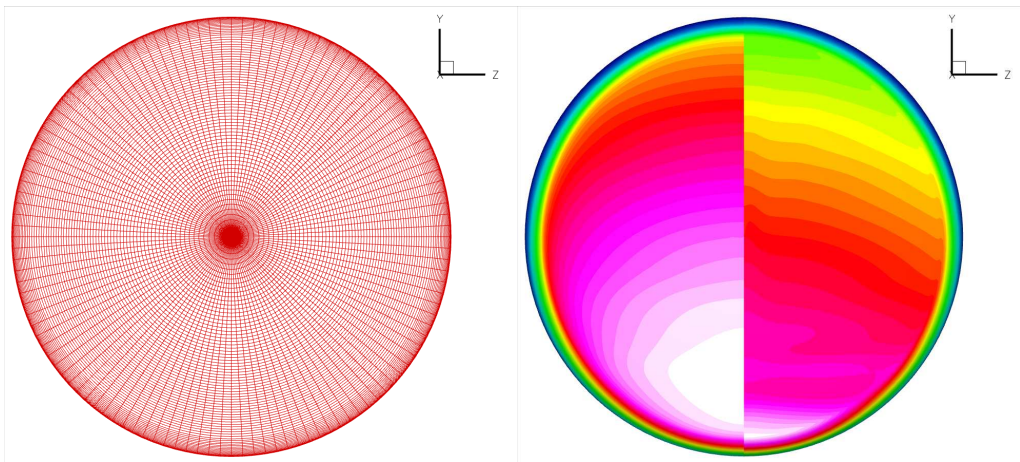
Figure 4.1 – *Axisymmetric grid on surface of Apollo Command Module-like shape; surface pressure (left) and heat flux (right).*
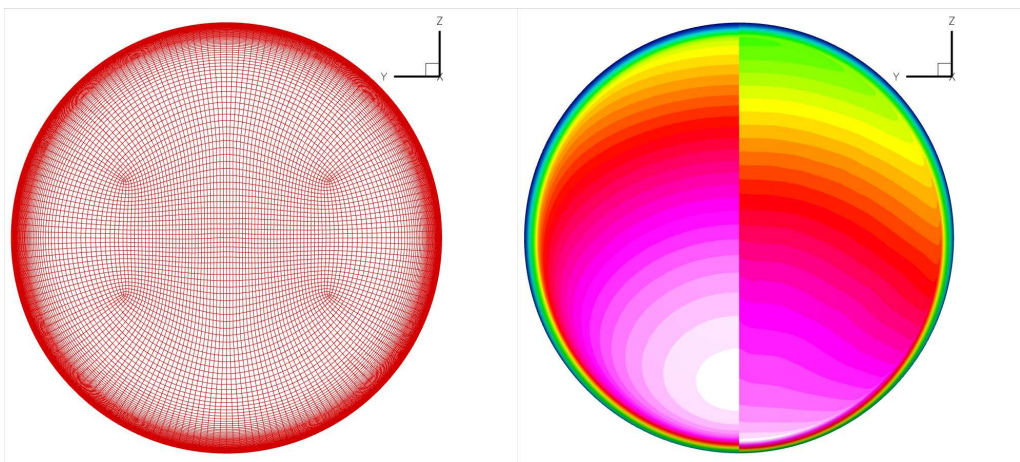
Figure 4.2 – *Patched grid on surface of Apollo Command Module-like shape; surface pressure (left) and heat flux (right).*

A better grid generation strategy is shown in Figure 4.2; here a patch is added at the nose, and a C-grid is wrapped around the patch. This results in more uniform grid spacing in the critical stagnation region. In addition, this grid has been adapted to the bow shock so that the error produced by the shock is reduced. We are now able to obtain a reasonable solution for this problem. Figure 4.2 plots the pressure and convective heat flux for the free-stream conditions given above. Note that heat flux no longer has a minimum near the stagnation point, unlike the result obtained on the previous grid.

The main conclusion to take from this brief comparison is that the solution in the stagnation region can be extremely grid sensitive (at least using the methods discussed here). Great care must be taken with grid generation, and for problems with large stagnation regions, the grid must be aligned with the shock wave to obtain reliable results. Furthermore, it is recommended that several numerical flux methods be used to assess the sensitivity of the results to the numerical approach.

The primary source of error is associated with how the strong bow shock crosses the grid. If there is perfect alignment, the CFD method exactly reproduces the shock jump conditions and there is no error. However, when the grid is not aligned with the shock, a spurious component of velocity tangent to the shock wave is produced. This error acts as a source of vorticity at the shock wave, which can accumulate in the stagnation region. Clearly methods that are less sensitive to grid orientation are needed and new work in multi-dimensional and rotated Riemann solvers may help reduce this dependence.

4.2 Double-Cone Flow

The double-cone flow field discussed in Section 1.1.1 is an interesting test case for evaluating numerical methods. In Figure 1.1, the separation zone that forms between the two conical sections is shown. The size of the separation zone can be detected in the heat flux and pressure measurements, as seen in Figures 1.2 and 1.3. The computed size of this separation zone is a direct measure of the quality of the numerical solution. Coarse grids produce a small separation, and numerical flux functions with large dissipation also under-predict the separation length. Thus, numerical methods can be evaluated by simulating the double-cone flow and comparing the size of the separation zone.

Figure 4.3 plots the separation zone length as a function of the grid spacing for a variety of numerical methods.[4] This plot shows that all of the methods converge to the

---

[4] This work was done in collaboration with Dr. Marie-Claude Druguet of IUSTI – École Polytechnique Universitaire de Marseille.

46

same separation zone length as the grid is refined. However, the rate of this convergence varies with the method, and for a given grid size the accuracy of each method is different. Furthermore, the effect of the slope limiter can be readily seen, with the superbee limiter providing more accurate results than the minmod limiter, for example. Therefore, making two simulations on different sized grids will give an immediate assessment of the accuracy of a numerical method. It should be noted that these calculations were performed with a perfect gas model without vibrational energy relaxation effects. Thus, the experimentally measured separation zone is different that those plotted here. See Ref. 16 for more details.

It is important to note that these flows take a long time to evolve, and it is important to carefully monitor the convergence to steady state. Physically, these flows take at least 150 flow times to converge, where one flow time is based on the free-stream speed and the length of the geometry (Ref. 19). Thus, time-like simulations must be computed for at least this length of time before the solution can be considered to be converged.
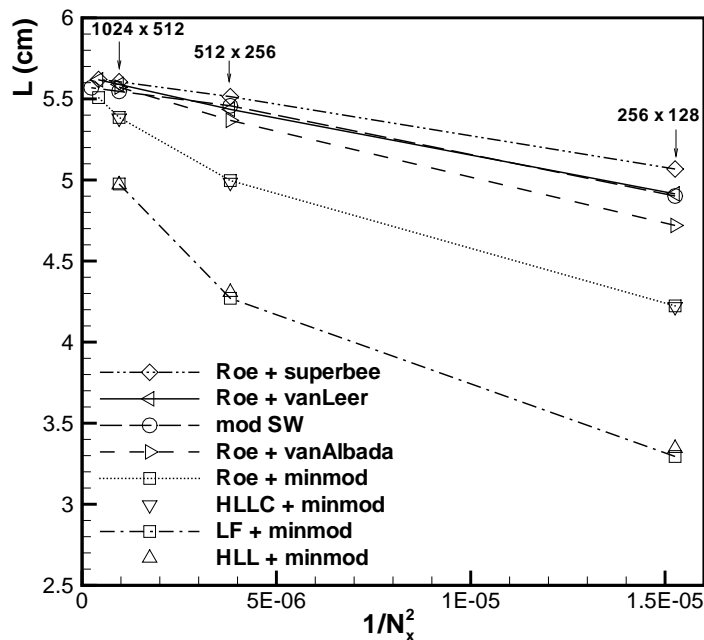
Figure 4.3 – *Size of the separation zone versus the square of the grid spacing in the streamwise direction (Ref. 16).*

4.3 Mach 8 Waverider Flow

A third example involves the simulation of a waverider geometry at Mach 8 conditions to compare with experimental measurements made in the AEDC Tunnel 9 facility (Ref. 15). These simulations were performed on three grids ranging in size from 2.5 to 8.5 million elements. The outer domain was designed to contain the bow shock wave at all angles of attack. Figure 4.4 shows some snapshots of the grid and waverider geometry. Two conditions were studied: a low Reynolds number of 14.32×10^6 /m and a high Reynolds number of 53.84×10^6 /m.

Natural transition occurs on the waverider at the lower Reynolds number condition. We did not attempt to model the transition process, but rather ran fully laminar and fully turbulent flows and compared those results with the experimental data. In the high Re case, transition occurs very near the leading edge, and therefore we ran fully turbulent only. Here, we use the Spalart-Allmaras RANS model with the Catris-Aupoix compressibility correction (Refs. 77, 11).

To a large extent the comparisons are very favorable, with the CFD matching the aerodynamic data across the angle of attack sweep at both conditions. For example, Figure 4.5 shows the lift and drag coefficients for the two cases. We also made comparisons with the individual pressure and heat transfer gauges on the model. Figure 4.6 summarizes one such comparison for the low Re condition on lower surface of the model (the windward surface at $\alpha > -5°$). Note the excellent agreement with the data, and that the thermocouple near the leading edge shows laminar flow, while all other measurements indicate turbulent flow.
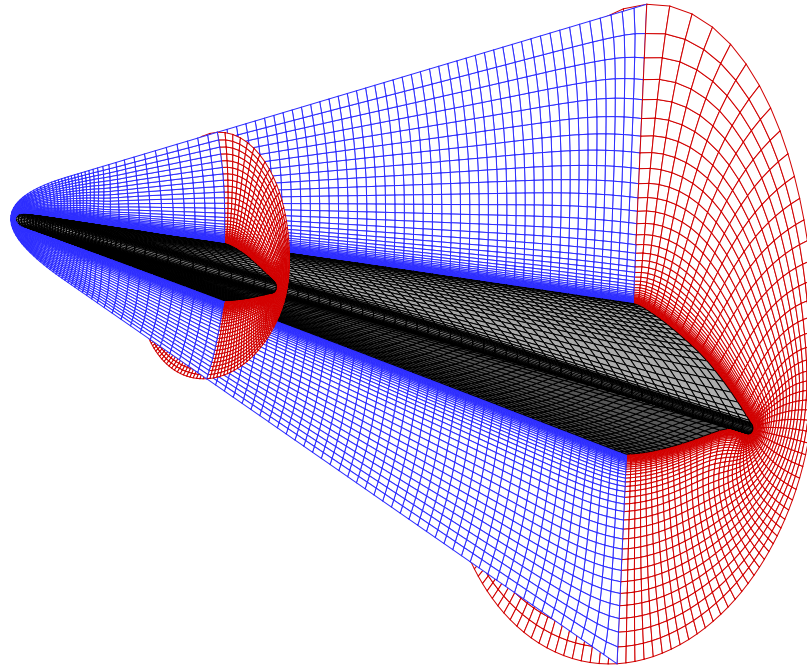
Figure 4.4 – *Medium grid (5.1 million elements) used for the waverider simulations; every second point shown (Ref. 15).*
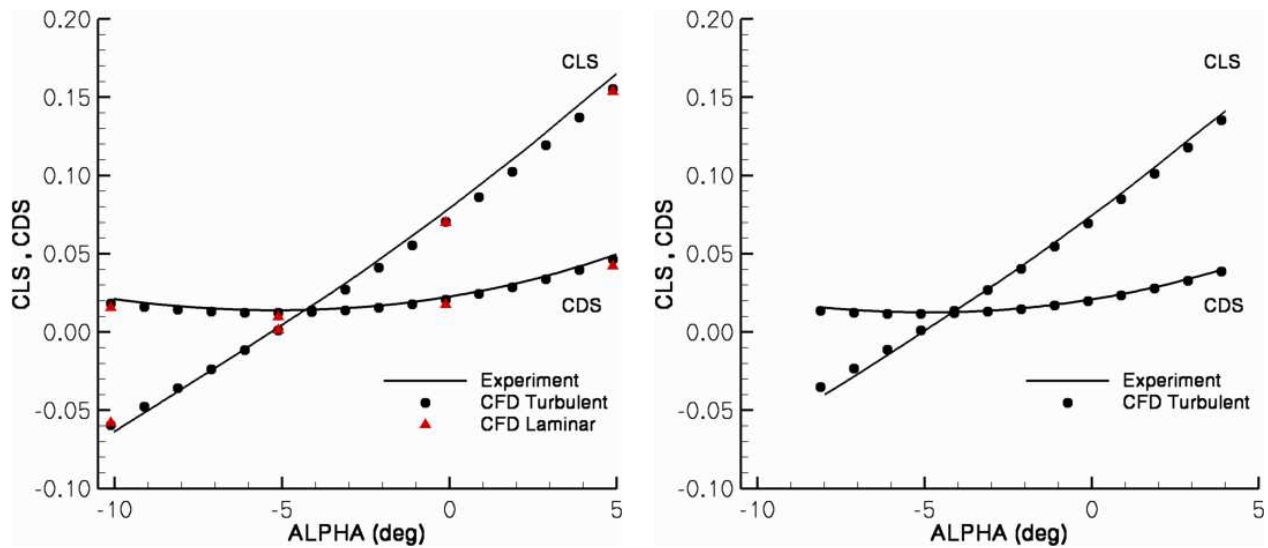

Figure 4.5 – *Lift and drag coefficients for the waverider at the low Re (left) and high Re (right) conditions.*
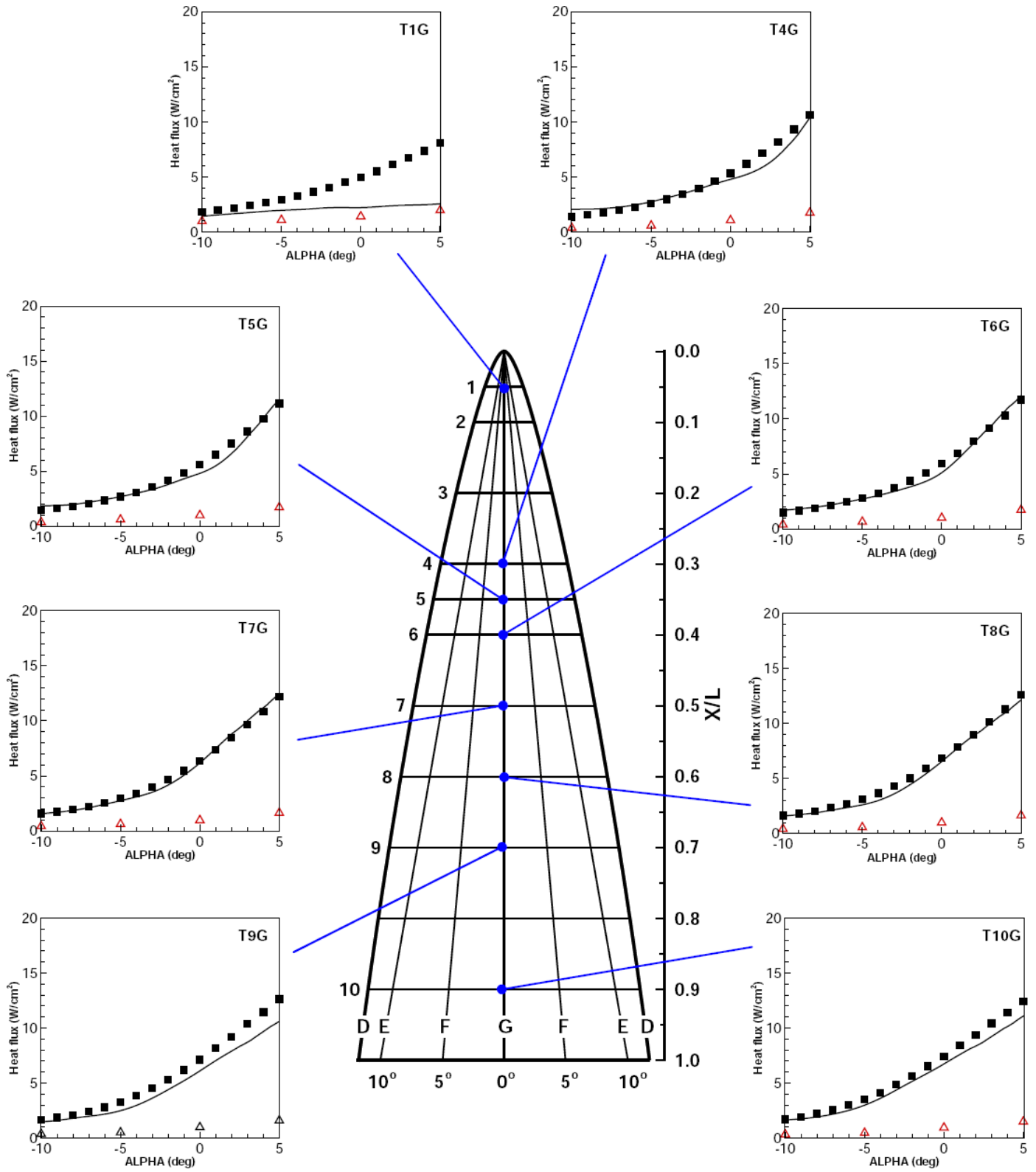
Figure 4.6 – *Heat transfer rate comparisons on the lower surface of the waverider at low Re.*

5. Hypersonic Nozzle Simulations

5.1 Introduction

Hypersonic vehicle development requires reliable ground-testing in a variety of facilities, such as high-pressure blow-down tunnels, high-enthalpy shock tunnels, and combustion-heated facilities. Because of the requirements for high enthalpy and high Reynolds number, all of these tunnels employ extreme reservoir conditions that may result in internal energy excitation, chemical reactions, and water vapor condensation. High Reynolds number facilities usually require reservoir conditions of hundreds of atmospheres, making the gas thermally imperfect. These non-ideal effects require advanced simulation methods to accurately predict the operating conditions of the tunnels.

Here, We discuss a computational fluid dynamics method for the simulation of hypersonic nozzles with high-pressure reservoir conditions and finite-rate vibrational relaxation and chemical reactions. We show that the single-parameter excluded-volume equation of state is valid for a wide range of hypersonic nozzle flows, and develop a consistent flux vector splitting approach for this model. The Spalart-Allmaras turbulence model with a compressibility correction is used to represent the nozzle boundary layer. The governing equations are integrated using a parallel implicit line-relaxation method that is very effective on the highly-stretched grids required to resolve high-pressure nozzle boundary layers. Grid convergence studies show little sensitivity of the results to grids larger than about 300×300 grid points (depending on the nozzle and flow conditions), resulting in rapid simulation times on parallel computers and clusters.

Comparisons with previous simulations and measurements for several facilities are presented. It is found that the nozzle simulation method over-predicts the high-pressure AEDC Tunnel 9 Pitot pressure measurements. However, a moderate pressure case agrees very well with previous simulations. The method also agrees very well with Pitot pressure surveys in the inner portion of the boundary layer, but over-predicts the Pitot pressure at the boundary layer edge. We investigate the effect of vibrational equilibrium, and find that it reduces the exit-plane Pitot pressure slightly, but not to the measured levels. The simulations are more encouraging for the CUBRC shock tunnels, with the method agreeing very well for Pitot pressure profiles across the entire nozzle exit plane. Comparisons with nozzle wall heat transfer rate are also very good for both Tunnel 9 and the CUBRC LENS-I shock tunnel.

5.2 Physical Models for Hypersonic Nozzle Flows

The nozzle simulation method is designed for the analysis of hypersonic converging-diverging nozzles including the effects of high pressure, finite-rate chemical reactions and vibrational relaxation, and turbulent wall boundary layers. In addition, a module has been written to predict the onset of water vapor condensation for hydrocarbon combustion product test gases. In the following section, the physical models are discussed.

5.2.1 High-Pressure Model

The nozzle simulation code uses the excluded volume thermal equation of state (also known as the Abel or Clausius equation of state). This is the first correction to the perfect gas equation of state, and it accounts for the volume occupied by the gas particles. The thermal equation of state is written as (Refs. 47, 80)

$$p = \frac{\rho R T}{1 - b_o \rho / \bar{M}} \tag{5.1}$$

where R is the mixture gas constant, b_o is the co-volume of the mixture, and $\bar{M}$ is the mixture average molecular weight. For a reacting gas, $b_o/\bar{M}$ is a constant, making the model depend on only a single parameter. b_o is obtained from the effective molecular diameter, σ, with

$$b_o = \frac{2}{3} \pi \sigma^3 N_o \tag{5.2}$$

where N_o is the Avogadro number.

Note that with this thermal equation of state, the internal energy, e, is a function of the temperature only, and that $c_p - c_v = R$, as for perfect gases. For the case where the ratio of specific heats, $\gamma = c_p/c_v$, is constant, an isentropic process is described by $p(\frac{1}{\rho} - b)^\gamma = \text{constant}$. Thus, we can compute the speed of sound, a, as

$$a^2 = \left.\frac{\partial p}{\partial \rho}\right|_s = \gamma \frac{1}{1 - \rho b} \frac{p}{\rho} \tag{5.3}$$

The specific enthalpy includes a contribution from the equation of state

$$h = e + p/\rho = e + \frac{RT}{1 - b_o \rho / \bar{M}} \tag{5.4}$$

and thus if the total enthalpy is used to set the reservoir conditions, this expression must be used.

For the case of high pressure nitrogen flows, we can use the empirical fit for pressure of Jacobsen *et al.* (Ref. 32) to determine the validity of the excluded volume approach.

This is a 33 parameter fit that is accurate to within 0.3% up to 150,000 psi and 3500 °R. Figure 5.1 plots the compressibility, $Z = p/\rho RT$, as a function of the pressure for various temperatures. Z measures the departure of the dense gas from the perfect gas equation of state. Note that Z differs from unity for conditions close to the critical point, and for very high pressures. (For nitrogen, the critical pressure and temperature are $p_c = 33.54$ atm and $T_c = 126.2$ K.)

Also plotted in Fig. 5.1, is the compressibility from the excluded-volume equation of state. We have taken $b_o/\bar{M} = 0.001120$ m³/kg by equating the pressures at a typical hypersonic nozzle reservoir condition ($p = 20,000$ psi, $T = 3400$ R). This value of $b_o/\bar{M}$ corresponds to an effective molecular diameter of $\sigma = 2.919$ Å, which is consistent with values from the literature at high temperature. Figure 5.1 shows that at high temperature the excluded volume approach is very accurate. However, at low temperature it is poor because it does not include the effect of attractive forces in the equation of state. Figure 5.1 also shows that at lower pressures the excluded volume approach agrees better, even for low temperatures.

Hypersonic nozzle flows start with a gas at high pressure and temperature, and then rapidly expand the gas to low pressure and temperature. Thus, in these flows there is never a situation where the pressure is high and the temperature is low. As a result, we expect the departure from the perfect gas equation of state to be largest in the reservoir. The gas never approaches its critical state because at temperatures close to the critical point, the pressure is always very much less than the critical pressure. For example, consider the expansion of 20,000 psi (137.9 MPa) and 3400 R (1889 K) nitrogen through a hypersonic nozzle to a Mach number of 14.1. We can take the density and temperature from a perfect gas nozzle calculation, and compute the pressure given by the Jacobsen *et al.* expression and Eq. (5.1). This gives an approximate variation of ρ and T for a typical hypersonic nozzle flow, and allows us to compare the two equations of state. The error is always less than 0.35%, which is very close to the 0.3% stated accuracy of the empirical fit.

Similarly for high pressure air flows, we can use the high accuracy fit of Lemmon *et al.* (Ref. 43). Figure 5.2 plots the same comparisons as given above using $b_o/\bar{M} = 0.001024$ m³/kg for air, corresponding to $\sigma = 2.86$ Å. This is very similar to the value of 2.9 Å used by Lordi and Mates for high temperature air. Figure 5.3 plots the error between the excluded volume equation of state and the Lemmon *et al.* fit for a wide range of temperatures and densities; also plotted is a typical variation of temperature and density for a hypersonic nozzle flow. This further shows that the excluded volume equation of state is poor for low temperatures at high densities. However, for the nozzle expansion, it is

within 0.4% of the complex (32 parameter) fit of Ref. 43, which has a stated accuracy of 0.5%. Lemmon *et al.* also give an expression for the speed of sound at high pressure, which we can compare to Eq. (5.3) in the hypersonic nozzle flow. Figure 5.4 shows this comparison; note that the error is very small, and most importantly at the sonic point, the error is only 0.01%. These comparisons show that the excluded volume approach is applicable to hypersonic nozzle flows.
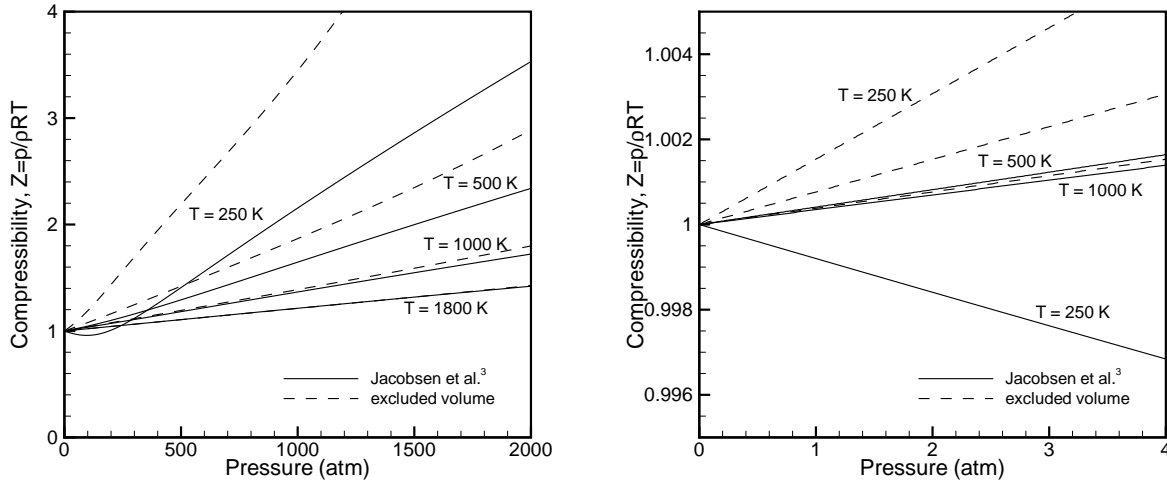

Figure 5.1 – *Comparison of compressibility from the high accuracy fit of Jacobsen et al. (Ref. 32) and the excluded volume approach for nitrogen; $b_o/\bar{M} = 0.001120\,\mathrm{m^3/kg}$.*
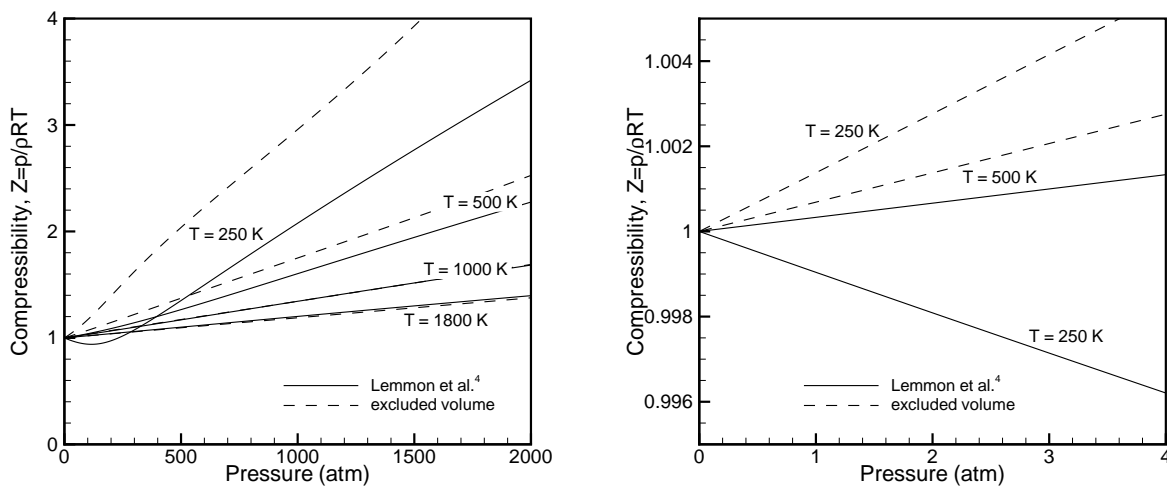
Figure 5.2 – *Comparison of compressibility from the high accuracy fit of Lemmon et al. (Ref. 43) and the excluded volume approach for air; $b_o/\bar{M} = 0.001024\,\mathrm{m^3/kg}$.*
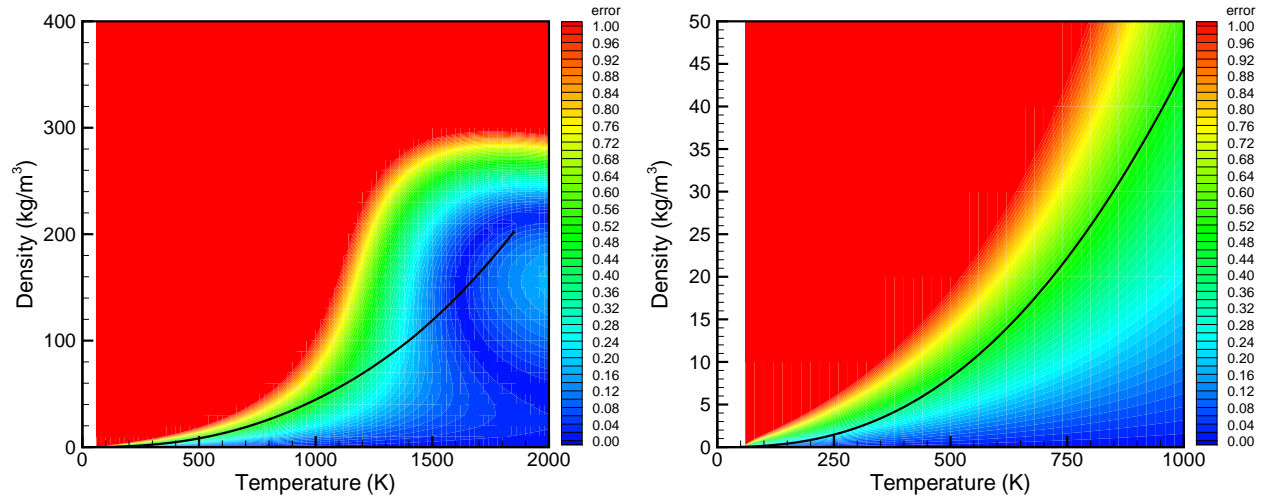
Figure 5.3 – *Per cent difference in computed pressure using the high accuracy equation of state (Ref. 43) and the excluded volume approach for the expansion of air in a hypersonic nozzle from* $20,000\,\mathrm{psi}$ *and* $3400\,°\mathrm{R}$ *to Mach 14.1.*
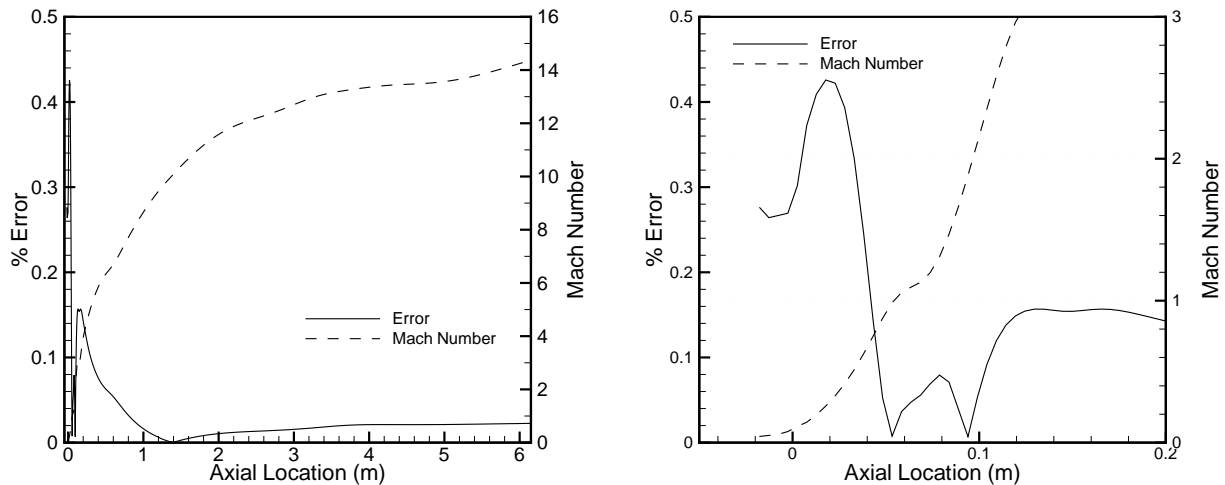

Figure 5.4 – *Per cent difference between the speed of sound from Ref. 43 and Eq. (5.3) for the expansion of air in a hypersonic nozzle from* $20,000\,\mathrm{psi}$ *and* $3400\,°\mathrm{R}$ *to Mach 14.1.*

For other gases, the effective molecular diameter may be obtained from various sources. The mixture value is then computed by number-weighting (or mole-weighting) the pure gas values:

$$\left.\frac{b_o}{\bar{M}}\right|_{\mathrm{mix}} = \frac{2}{3}\pi N_o \sum_s \gamma_s \frac{\sigma_s^3}{M_s} \tag{5.5}$$

where the sum is over all species, and γ_s is the mole fraction of species s.

5.2.2 Internal Energy

In hypersonic nozzle flows, the vibrational energy modes of the gas are often excited. The nozzle code models the vibrational excitation using a simple harmonic oscillator, which is valid for typical reservoir temperatures. The gas mixture vibrational energy per unit volume, E_v, is given by

$$E_v = \sum_s \rho_s e_{vs} \tag{5.6}$$

where the vibrational energy for each species is

$$e_{vs} = \frac{R}{M_s} \sum_r g_{rs} \frac{\theta_{vrs}}{\exp(\theta_{vrs}/T_v) - 1} \tag{5.7}$$

where r is summed over each vibrational mode of species s, θ_{vrs} is the characteristic temperature of vibration for that mode, and g_{rs} is the degeneracy of that mode. These constants are well known and are available from sources such as the NIST-JANAF Thermochemical Tables (Ref. 12). In the above expression, T_v is the vibrational temperature that characterizes the gas mixture. Thus, we have assumed that the vibrational modes of the gas relax with one another relatively quickly, resulting in a single vibrational temperature.

The vibrational energy modes are assumed to relax toward the translational modes using the Landau-Teller model. We compute a number-weighted relaxation time using the individual species relaxation times from Millikan and White (Ref. 57). This model is accurate for most species pairs, however it is known to be inadequate for carbon dioxide relaxation because of resonant energy transfer between modes. Therefore, we use the results of Camac (Ref. 7) to improve the vibrational energy relaxation model when carbon dioxide is present.

To construct the total energy per unit volume of the mixture, E, we sum the translational-rotational energy, the vibrational energy, and the kinetic energy

$$E = \sum_s \rho_s c_{vs} T + E_v + \frac{1}{2}\rho(u^2 + v^2) + \sum_s \rho_s h_s^o \tag{5.8}$$

where c_{vs} is the translational-rotational specific heat at constant volume for species s. For example, diatomic molecules have $c_{vs} = \frac{5}{2}\frac{R}{M_s}$, and atoms $c_{vs} = \frac{3}{2}\frac{R}{M_s}$. h_s^o is the heat of formation of species s. Thus this model includes all relevant energy storage modes: the translational and rotational modes are assumed to be in equilibrium with one another, vibrational modes are characterized by a single temperature T_v, and chemical energy is allowed to evolve according to an appropriate finite-rate chemical kinetics model.

5.2.3 Finite-Rate Chemical Reactions

The chemical composition of the gas changes as it flows through the converging-diverging nozzle. In many cases, the expansion is so sudden that a chemical equilibrium assumption is not valid, and we must consider finite-rate recombination of the test gas. To do so, we solve a mass conservation equation for each chemical species, including a mass production or destruction term due to chemical reactions. The equation is

$$\frac{\partial \rho_s}{\partial t} + \frac{\partial}{\partial x_j}\big(\rho_s u_j + \rho_s v_{sj}\big) = w_s \tag{5.9}$$

where we have used index notation. Here v_{sj} is the diffusion velocity of species s relative to the mass-averaged velocity, u_j. w_s is the chemical source term due to reactions; this is constructed from the law of mass action and an appropriate chemical kinetics model.

For typical hydrocarbon reaction products, we consider an 11-species CHON model consisting of CO_2, H_2O, CO, N_2, O_2, H_2, OH, O, H, and N. The kinetics model used is based on rates taken from the Gas Research Institute Mechanism 3.0 (GRI-Mech3.0) (Ref. 27). For air flows, we use a 5-species model with 5 reactions; and for a pure nitrogen flow we just use the nitrogen dissociation/recombination reaction.

The forward reaction rates for each of these reactions is from GRI-Mech3.0, and we compute the backward rates using the forward rate and the equilibrium constant. We curve fit the equilibrium constant using a five-parameter fit over the temperature range of interest by minimizing the Gibbs free energy based on the Gordon and McBride thermochemical data (Ref. 23). The curve fits provided with the code are valid in the range $200 \leq T \leq 3200\,\mathrm{K}$; a different temperature range can be fit with minimal effort as needed. All equilibrium constants have been verified by comparison with the GRIMech3.0 tabulations.

5.2.4 Transport Properties and Turbulence Modeling

The molecular viscosity, thermal conductivity, and mass diffusivity are computed using the Wilke mixing rule (Ref. 84), with pure species data obtained from the Blottner curve fits (Ref. 3). All relevant data are provided in the input files for the nozzle simulation code. In the case of nitrogen gas, the viscosity fits from Ref. 20:

$$\mu = \begin{cases} 2.8676 \times 10^{-8}\,T^{0.979} & T \leq 227\,\mathrm{R}; \\ 6.8971 \times 10^{-7}\,T^{1.5}/(179.1 + T) & 227 < T \leq 795\,\mathrm{R}; \\ 1.9466 \times 10^{-7}\,T^{0.659} & T > 795\,\mathrm{R}. \end{cases} \tag{5.10}$$

where T is in Rankine and μ is in lbm/ft s (multiply by 1.4882 to obtain SI units of kg/m s).

The translational-rotational thermal conductivity is obtained through the use of an Eucken relation, which is essentially a variation of the Prandtl number to account for the mixture of different components. The thermal conductivity of pure species s is

$$k_s = \mu_s \left(\frac{9}{4} + c_{vs} \right) \frac{R}{M_s}. \tag{5.11}$$

The mixture value is then obtained using the Wilke mixing approach. The vibrational energy conduction is written as:

$$q_{vj} = \sum_s \eta_v \mu_s \frac{\partial e_{vs}}{\partial x_j} \tag{5.12}$$

which is more accurate and stable than basing the vibrational heat flux on the vibrational temperature. The value of η_v is taken to be 1.2 from Ref. 60. The mass diffusivity is based on simple Fickian diffusion with a constant Lewis or Schmidt number.

It is critical to predict the correct boundary layer thickness in hypersonic nozzles because it determines the effective area ratio of the nozzle, and therefore the facility operating conditions. In hypersonic facilities, the nozzle wall boundary layers are almost always turbulent because of the extremely high unit Reynolds number in the throat region. However, conventional algebraic turbulence models (*e.g.* Baldwin-Lomax) do not work well because of the highly favorable pressure gradient and strong temperature gradients in the boundary layer. We have performed extensive comparisons between Pitot pressure rake measurements and nozzle wall heat transfer rate measurements in the CUBRC LENS facilities (Ref. 58). We find that the one-equation Spalart-Allmaras turbulence model (Ref. 77) with the Catris and Aupoix compressibility correction (Ref. 11) gives good agreement with experiments across a wide range of nozzle operating conditions.

5.2.5 Boundary Conditions

The nozzle wall boundary conditions are straight-forward: no-slip for velocity and either adiabatic or isothermal for the wall temperature. In the isothermal case, either the wall temperature can be set to a single value (appropriate for a short-duration impulse facility), or to values obtained from surface temperature measurements during tunnel operation (for a longer-duration blow-down tunnel).

The inflow boundary condition is more difficult to define because of vibrational excitation and the imperfect equation of state. We found that a characteristic-based inflow boundary condition does not conserve the inflow stagnation properties. Here, a different approach is used: the total mass flux across a plane of the interior solution is computed,

and the inflow velocity is then set so that the inflow has that mass flux; the temperature is then adjusted to maintain the specified stagnation enthalpy of the inflow based on assuming that the density varies only weakly as the gas accelerates. This approach then assures that the inflow stagnation conditions are correctly specified and that once the nozzle has choked, the mass flow through the inlet is correct. Extensive testing has validated this approach.

5.3 Governing Equations for Hypersonic Nozzle Flows

The flow in a hypersonic nozzle is described by the Navier-Stokes equations, along with a conservation equation for the vibrational energy. For high enthalpy shock tunnels, the gas in the reservoir may be dissociated, in which case, mass conservation equations for each possible chemical species must be included as well. Here we just consider the non-reacting case, but the extension to multiple species is straight-forward as discussed in section 2.

For an axisymmetric flow, the governing equations may be written as

$$\frac{\partial U}{\partial t} + \frac{\partial F}{\partial x} + \frac{1}{y}\frac{\partial yG}{\partial y} = W, \tag{5.20}$$

where x is the axial direction and y is the distance from the nozzle axis. For this flow, we have

$$U = \begin{pmatrix} \rho \\ \rho u \\ \rho v \\ E_v \\ E \end{pmatrix}, \quad W = \begin{pmatrix} 0 \\ 0 \\ (p + \tau_{\theta\theta})/y \\ Q_v \\ 0 \end{pmatrix}$$

$$F = \begin{pmatrix} \rho u \\ \rho u^2 + p - \tau_{xx} \\ \rho uv - \tau_{xy} \\ E_v u + q_{vx} \\ (E + p - \tau_{xx})u - \tau_{xy}v + q_x \end{pmatrix} \tag{5.21}$$

$$G = \begin{pmatrix} \rho v \\ \rho uv - \tau_{yx} \\ \rho v^2 + p - \tau_{yy} \\ E_v v + q_{vy} \\ (E + p - \tau_{yy})v - \tau_{yx}u + q_y \end{pmatrix}$$

The first three equations in Eq. (5.20) are the continuity and momentum equations for an axisymmetric flow. The fourth equation describes the conservation of vibrational energy

per unit volume, E_v, with a finite-rate relaxation source term, Q_v. The final equation is the total energy conservation equation, with E, the total energy per unit volume, given by

$$E = \rho c_v T + E_v + \frac{1}{2}\rho(u^2 + v^2),\tag{5.22}$$

with c_v the specific heat at constant volume, $c_v = \frac{5}{2}R$ for a diatomic gas. The vibrational energy is written in terms of the vibrational temperature, T_v. For most flows, a simple harmonic oscillator model is adequate, with $E_v = \sum \rho_s e_{vs}$. The source term is obtained from the Landau-Teller model

$$Q_v = \frac{E_v^*(T) - E_v}{\tau_v},\tag{5.23}$$

where E_v^* is the vibrational energy evaluated at the translational-rotational temperature T, and τ_v is the vibrational relaxation time.

We use the excluded volume equation of state, Eq. (5.1), to relate the pressure to the local density and temperature. The stresses and heat fluxes are computed using standard expressions for the Navier-Stokes equations and expressions for the transport properties. In the case of turbulent flow in the nozzle, the turbulent transport may be included with a turbulence model in the usual fashion. We use the Spalart-Allmaras one-equation turbulence model with the Catris and Aupoix compressibility correction. We assume that the nozzle boundary layer is fully turbulent because of the extremely high Reynolds numbers in the high-pressure throat region.

5.4 Computational Method

The governing equations may be solved with many different computational fluid dynamics methods. We choose to use a finite-volume approach with a modified version of Steger-Warming flux vector splitting (Refs. 8, 9, 50, 52). Below we derive an extension of this method for the non-ideal equation of state; other methods for gas dynamics may be extended in a similar fashion.

The development of the flux vector splitting method for perfect gases uses the fact that the inviscid flux vectors are homogeneous of order one in the vector of conserved variables, U. In this case, the inviscid flux in the x direction, F_I, for example, may be written

$$F_I = \frac{\partial F_I}{\partial U}U = AU\tag{5.24}$$

The inviscid flux Jacobian, A, has a complete set of real eigenvalues and may be diagonalized. Thus we split the flux into its forward and backward moving components according

to the sign of the eigenvalues of A. We write this as $F_I = A_+U + A_-U$, and upwind data are used to evaluate this expression.

For the imperfect gas, F is not homogeneous in U, and Eq. (5.24) does not hold. Note that the x-direction inviscid flux Jacobian is

$$A = \frac{\partial F_I}{\partial U} = \begin{pmatrix} 0 & u & 0 & 0 & 0 \\ -u^2 + p_\rho & 2u + p_{\rho u} & p_{\rho v} & p_{E_v} & p_E \\ -uv & v & u & 0 & 0 \\ -E_v u & e_v & 0 & u & 0 \\ -H + up_\rho & H + up_{\rho u} & up_{\rho v} & up_{E_v} & u + up_E \end{pmatrix} \tag{5.25}$$

where $H = (E + p)/\rho$ is the specific total enthalpy, and the subscripts on p denote partial derivatives of p. The product of A with U is

$$AU = \begin{pmatrix} \rho u \\ \rho u^2 + \frac{\partial p}{\partial U_i} U_i \\ \rho uv \\ E_v u \\ Eu + u\frac{\partial p}{\partial U_i} U_i \end{pmatrix} \tag{5.26}$$

where $\frac{\partial p}{\partial U_i} U_i = \frac{\partial p}{\partial \rho}\rho + \frac{\partial p}{\partial \rho u}\rho u + \frac{\partial p}{\partial \rho v}\rho v + \frac{\partial p}{\partial E_v}E_v + \frac{\partial p}{\partial E}E$. Clearly, if this quantity is equal to p, then $F_I = AU$ and conventional flux vector splitting approach may be used. For the case of the excluded volume equation of state, we compute

$$\frac{\partial p}{\partial U_i} U_i = p\left(1 + \frac{\rho b}{1 - \rho b}\right) \tag{5.27}$$

and thus $F_I \neq AU$.

In this case, we follow the approach of Liou et $al.$ (Refs. 45, 46) and construct a Jacobian matrix, A_e, such that $F_I = A_eU$ and define A_ρ such that $A = A_e + A_\rho$. Then we have

$$F_I = A_eU$$
$$= AU - A_\rho U \tag{5.28}$$
$$= A_+ + A_- - A_\rho U$$

where we have diagonalized A, as discussed above. The Jacobians A_e and A_ρ can be found by considering the form of (5.27). An appropriate choice of A_ρ is

$$A_\rho = \begin{pmatrix} 0 & 0 & 0 & 0 & 0 \\ p\frac{b}{1-\rho b} & 0 & 0 & 0 & 0 \\ 0 & 0 & 0 & 0 & 0 \\ 0 & 0 & 0 & 0 & 0 \\ up\frac{b}{1-\rho b} & 0 & 0 & 0 & 0 \end{pmatrix}. \tag{5.29}$$

When we multiply this quantity by U, we obtain

$$F_\rho = A_\rho U = p\frac{\rho b}{1 - \rho b} \begin{pmatrix} 0 \\ 1 \\ 0 \\ 0 \\ u \end{pmatrix} \tag{5.30}$$

which makes $(A - A_\rho)U = A_e U = F_I$ as required. Note that A_ρ has eigenvalues that are zero, and thus we can use cell-averaged data for its evaluation.

When we diagonalize the Jacobian A, we find eigenvalues given by u, $u \pm a$, where the speed of sound a, is the same as Eq. (3). With the finite-rate vibrational relaxation model used here, the ratio of specific heats is given by $\gamma = 1 + \frac{R}{c_v}$ ($\gamma = \frac{7}{5}$ for a diatomic gas). This corresponds to a vibrationally frozen speed of sound.

The time-dependent governing equations are solved using the Data-Parallel Line-Relaxation method (Ref. 86), which is a parallelizable implicit method ideally suited to nozzle flow simulations. The method linearizes the fluxes in time, and solves the resulting linear system of equations along lines normal to the nozzle surface. This allows high Reynolds number problems to be solved in a relatively small number of time steps on very highly stretched grids. Results will be shown to illustrate the efficacy of the method.

5.5 Hypersonic Nozzle Simulations

5.5.1 AEDC Tunnel 9 Simulations

The first example will be used to verify that the computational method produces results that are consistent with previous simulations. Korte *et al.* (Ref. 39) performed a careful analysis of the AEDC Tunnel 9 Mach 14 nozzle at two conditions. The results did not agree well with experimental Pitot pressure surveys, however these calculations provide a good dataset for comparison purposes.

Korte *et al.* use a similar model to that employed in the present work, except that they assume vibrational equilibrium during the nozzle expansion. They use the same excluded volume equation of state with a value of $b_o/\bar{M} = 0.001117\,\mathrm{m}^3/\mathrm{kg}$ for nitrogen (compared to $0.001120\,\mathrm{m}^3/\mathrm{kg}$ used here). Korte performed a series of grid resolution studies and investigated uncertainties in the modeling and measurements to assess the reasons for the 6% to 9% differences in computed and measured Pitot pressures at the nozzle exit plane.

In the present work, we have performed a careful grid resolution study for the high-pressure case studied by Korte *et al.* In general, we do not see as strong sensitivity to

the grid resolution as shown they found. We generate grids by spline fitting between the Tunnel 9 Nozzle contour data. The grid is exponentially stretched to the nozzle wall to resolve the very thin near-wall turbulent boundary layer. For this case, we choose a wall grid spacing of 10^{-6} of the throat radius at the throat; at other axial locations the grid is scaled by the local nozzle radius. This results in a y^+ value of unity at the throat for the high pressure test case, and $y^+ < 1$ for all other locations. The axial direction grid spacing is chosen to be smoothly varying, with clustering near the throat.

The Tunnel 9 nozzle is over 12 m in length, with a throat radius of 0.5020 inch (1.275 cm). We can compute the characteristic time step size for this problem by using the throat grid spacing and the throat wall temperature to compute the near-wall speed of sound. This then gives

$$\Delta t_{\text{throat}} = \Delta n / a_{\text{throat}} = 1.5 \times 10^{-11} \, \text{sec}$$

for the high pressure case. The nozzle starting time can be estimated from the throat speed of sound and the length of the nozzle, which results in approximately 15 millisec, or a ratio of characteristic times of 10^9. There is a correspondingly large range of length scales because of the extremely thin boundary layer at the throat. This results in extremely large cell aspect ratios for the near-wall grid. (The cell aspect ratio is the ratio of the length to the height of a finite volume grid.) Here typical cell aspect ratios are on the order of 10^5. This extreme stretching causes difficulties for many implicit methods.

The present simulations were run with the DPLR implicit method that is designed for high Reynolds number flows with extreme grid stretching. In this case, we run at time steps 6 orders of magnitude larger than the characteristic time scale at the throat. Time steps of 5 microsec are typical, resulting in machine zero convergence in approximately 2000 time steps. Figure 5.5 plots the L_2 norm of the density residual for a typical simulation. Note that the Tunnel 9 nozzle is very long, which tends to increase the number of time steps required to start the nozzle and drive the residual to zero.

We consider the two cases studied by Korte *et al*: Run 2209 was at a high pressure condition of $20,872$ psia and $3332\,^\circ$R (143.9 MPa and 1851.1 K); and Run 2267 at a moderate pressure condition of $8,410$ psia and $2726\,^\circ$R (57.97 MPa and 1514.4 K). The wall temperature distribution was obtained from Ref. 39 for Run 2209, and was scaled by the relative reservoir temperatures for Run 2267.
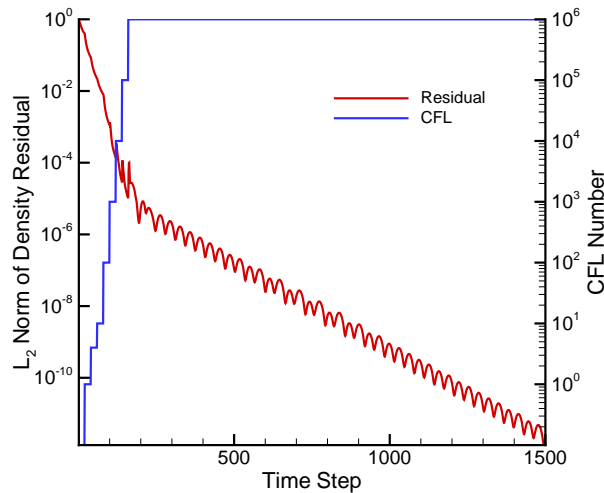
Figure 5.5 – L_2 norm of the density residual for the Tunnel 9 calculation; 300×120 grid.

Figure 5.6 plots the computed exit plane (492 inch station) Pitot pressure for Run 2209 conditions for various grids. The full Pitot pressure profile shows little difference between the solutions, except at the boundary layer edge where the coarser grids predict an overshoot in the Pitot pressure. The zoomed plot shows this difference more clearly; it also shows that all but the coarse grid (300×120) solution predict essentially the same centerline Pitot pressure. It should be noted that no attempt was made to optimize any given grid. Rather, the surface grid resolution was held fixed, and the grid points were distributed using stretching functions. This results in an excessive number of grid points in the boundary layer for many of the grids. It is very likely that a more intelligent design of the grid would result in a significantly reduced number of grid points. In all simulations the centerline total enthalpy is conserved to within 0.056%.

Figure 5.7 plots the computed Pitot pressure against that obtained by Korte *et al.* and measured in Tunnel 9. At Run 2209 conditions, the present results give substantially larger (6%) Pitot pressure than Korte, which also over-predict the experimental data (9%). Recent work in the AEDC Tunnel 9 facility used coherent anti-Stokes Raman spectroscopy (CARS) to measure the vibrational state of the test gas (Ref. 76). No vibrational nonequilibrium could be detected in that work, indicating that the vibrational relaxation may be faster in the tunnel than predicted in the present work. (Here the vibrational temperature is predicted to be 1446, K compared to the translational-rotational temperature of 49.0 K.) Therefore, computed the nozzle flow with the nonequilibrium model using a relaxation rate 10^8 faster than given by Ref. 57. This result is also plotted in Fig. 5.7, and causes the gas to closely approach vibrational equilibrium, resulting in a slight reduction of the pre-

dicted Pitot pressure (1.4%). Strictly speaking, this approach does not replicate a thermal equilibrium model because it does not use a temperature-dependent effective γ. That is in Eq. (5.3) $\gamma = c_p/c_v$, where $c_v = \frac{\partial e}{\partial T}\big|_v$ and $c_p = \frac{\partial h}{\partial T}\big|_p$. For a nonequilibrium model for pure nitrogen, γ has a constant value $\frac{7}{5}$. On the other hand, an equilibrium model results in a variable γ, which presumably could affect the throat speed of sound, and therefore the entire expansion process. Therefore, the nozzle code was modified to implement the thermo-chemical model used by Korte. We extended the derivation discussed above to allow for a general equation of state, resulting in a modified flux vector splitting formulation. This is different than the "effective γ" approach used by Korte, that simply replaces the ratio of specific heats with $\Gamma = h/e$.
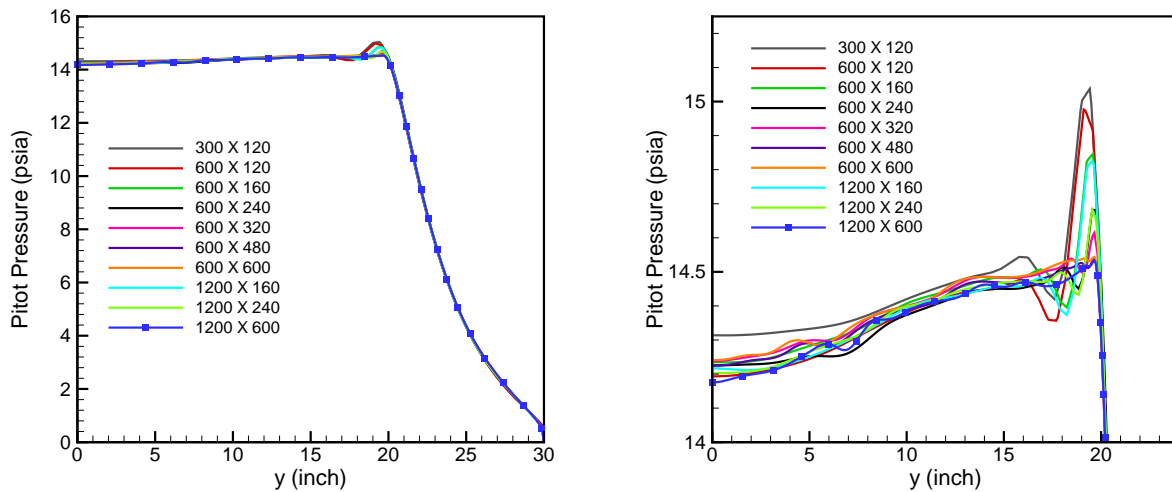

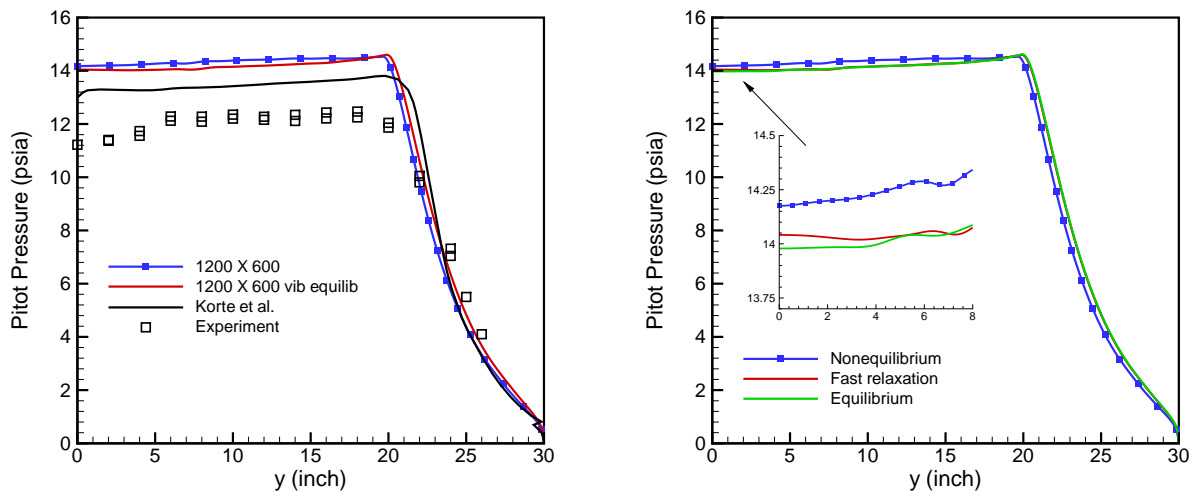Figure 5.6 – *Computed exit plane Pitot pressure for Run 2209 conditions.*

Figure 5.7 – *Computed exit plane Pitot pressure for Run 2209.*

In Korte's model, the constant volume specific heat, c_v, depends only on temperature, and is a curve fit to tabulated data. For this model, γ varies from 1.305 at typical throat conditions to 1.4 at the nozzle exit plane. It should be noted that the model used by Korte fits nitrogen with vibrational energy characterized by $\theta_v = 3264\,\mathrm{K}$ in Eq. (5.7). This is different than more commonly used value of $\theta_v = 3395\,\mathrm{K}$ for nitrogen (Ref. 68), however simulations with this different value of θ_v do not make an appreciable difference.

In any case, Figure 5.7 also plots the results of the equilibrium calculation using Korte's model. Note that the cases with vibrational equilibrium agree with one another, both in terms of the centerline Pitot pressure and the Pitot pressure in the boundary layer. This is an interesting result that merits further investigation, given the inherent differences in the two formulations. The main remaining difference between the present calculations and those of Korte is the turbulence model. Their calculations used the algebraic Cebeci-Smith and Baldwin-Lomax turbulence models, and showed more sensitivity to the grid resolution than the present results.

Figure 5.8 plots the results for the lower pressure and temperature Run 2267. Note the excellent agreement between the present simulations and those of Korte, particularly when the vibrational relaxation is accelerated. Again the simulations over-predict the experimental data by about 6%. The reason for this difference is currently unknown.

We also compared nozzle simulations to detailed near-wall Pitot pressure surveys taken by Jones (Ref. 34). Figure 5.9 plots this comparison for two high-pressure runs (20,000 psia and 3310 °R). The agreement is good near the surface, but again the simulations over-predict the Pitot pressure in the core of the nozzle flow.

Figure 5.10 plots the measured and computed heat flux to the Tunnel 9 nozzle wall at high pressure conditions (20,100 psia and 3180 °R). The agreement is remarkably good at all locations on the nozzle wall.

If the expansion is isentropic and adiabatic, the effective area ratio of the nozzle uniquely determines the exit conditions. The Pitot pressure profile is not a particularly sensitive measure of the boundary layer displacement thickness. But the comparisons do not show an egregious error that would result in a significant difference in the effective area ratio.
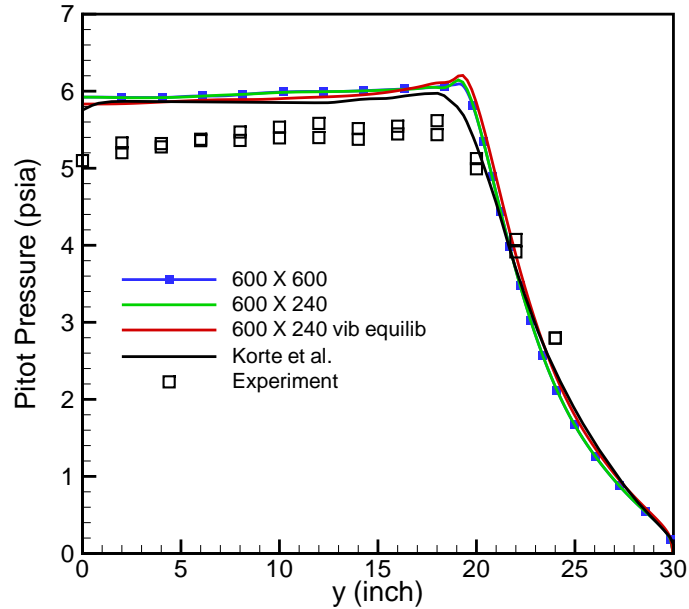
Figure 5.8 – *Computed exit plane Pitot pressure for Run 2267. Comparison with Korte et al. (Ref. 39) simulations and experimental measurements.*
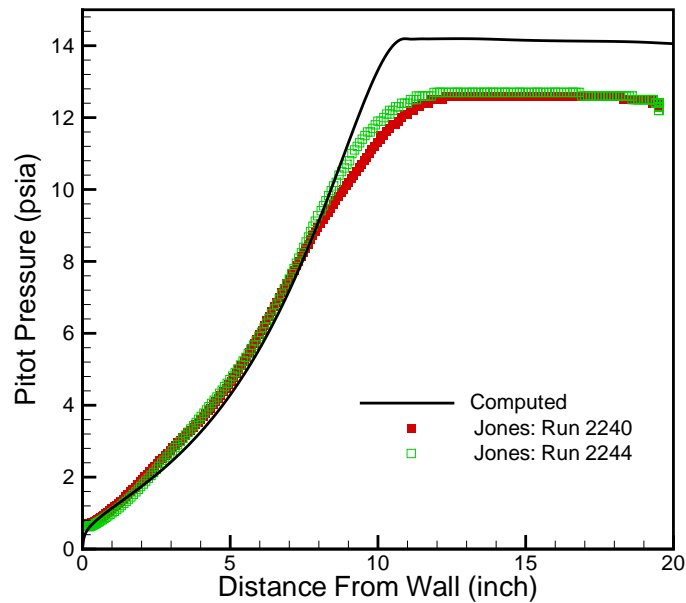
Figure 5.9 – *Comparison of computed and measured Pitot pressure in the boundary layer of the Tunnel 9 nozzle at Run 2240 and 2244 conditions. Comparison with experiments of Jones (Ref. 34).*
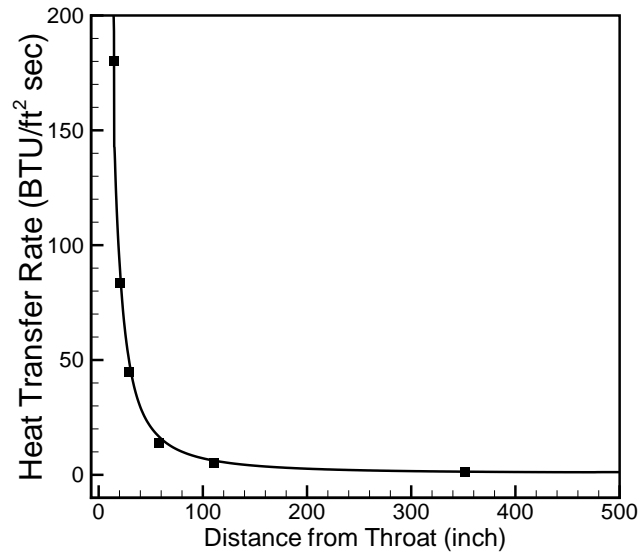
Figure 5.10 – *Comparison of computed and measured nozzle wall heat transfer rate for Tunnel 9 operating at* 20, 100 psia *and* 3180 °R*.

5.5.2 CUBRC LENS Facility Simulations

We have made extensive simulations of the Calspan-University at Buffalo (CUBRC) Large Energy National Shock Tunnel (LENS) facilities during the past several years. Reference 54 documents much of this work, and this section provides some typical results of the nozzle simulations. The CUBRC facilities operate at higher reservoir temperatures than AEDC Tunnel 9, and use air, nitrogen, and carbon dioxide as test gases. Thus, more complex thermo-chemical models must be used, including finite-rate chemical reactions. The present nozzle simulation code includes relevant kinetic models.

Figure 5.11 plots exit plane Pitot pressure comparisons for two nitrogen cases: Run 187 (190.6 atm and 6283 K) and Run 1302 (34.97 atm and 3083 K). Note that the agreement is excellent for both cases, with the simulations agreeing to within the scatter of the data. Figure 5.12 plots a comparison of the heat transfer rate to the nozzle wall for Run 187 conditions; again the agreement is excellent. The reason for this good agreement for the CUBRC LENS facility Pitot pressure surveys and poor agreement for AEDC Tunnel 9 is not known at this point.
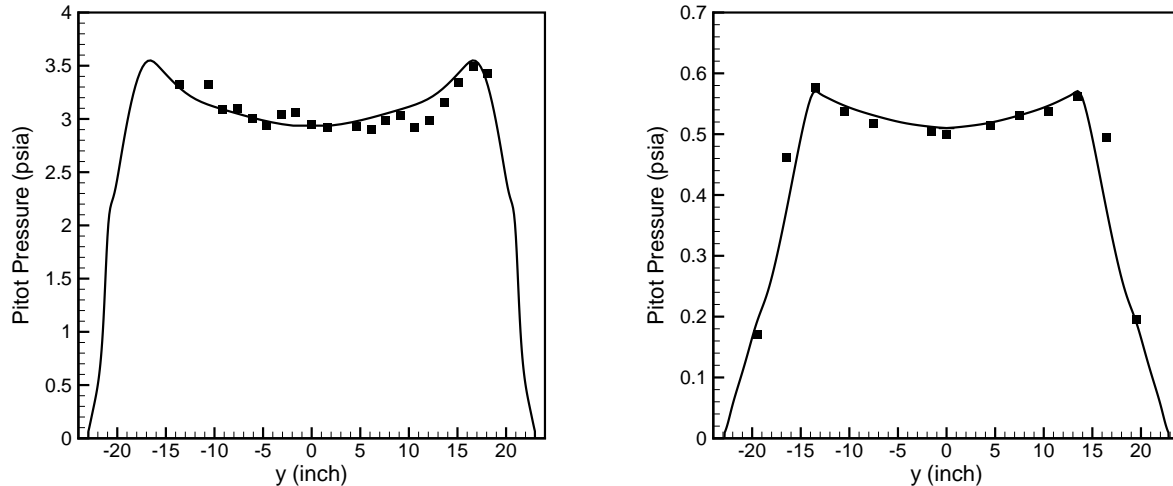
Figure 5.11 – *Comparison of computed and measured exit plane Pitot pressure for Run 187 (left) and Run 1302 (right) in CUBRC shock tunnel facilities.*
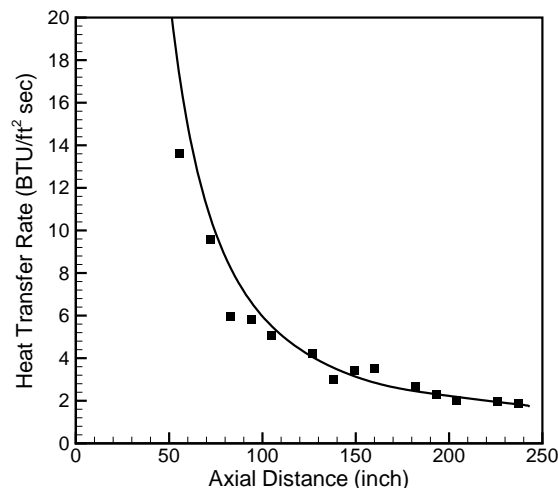

Figure 5.12 – *Comparison of computed and measured nozzle wall heat transfer rate for LENS-I at Run 187 conditions.*

5.5.3 NASA Langley 8′HTT Simulations

We have also considered the expansion of hydrocarbon combustion products through the NASA Langley 8-Foot High-Temperature Tunnel (8′HTT) for conditions taken from the work of Erickson *et al.* (Ref. 17) We use an 11-species finite-rate hydrocarbon model based on the Gas Research Institute reaction mechanism, GRI-Mech3.0 (Ref.27). We have considered Case 1 from Ref. 17, generated a 380×128 grid based on the nozzle contour

provided, and computed the flow field assuming equilibrium in the reservoir at $1900\,\mathrm{K}$ and $5\,\mathrm{MPa}$ ($3420\,\mathrm{R}$ and $725\,\mathrm{psi}$). Figure 5.13 plots the temperatures and pressure along the nozzle centerline for this case; agreement is reasonable in comparison to the limited information available from Ref. 17. Using the formulae provided by Erickson *et al.* the saturation temperature and nucleation rate are also computed and plotted in Fig. 5.13; agreement is also good, with the gas becoming saturated at the same point ($x = 6.8\,\mathrm{m}$). The present nonequilibrium calculations predict an earlier and larger nucleation rate than the previous equilibrium results; this is consistent with the modeling differences.
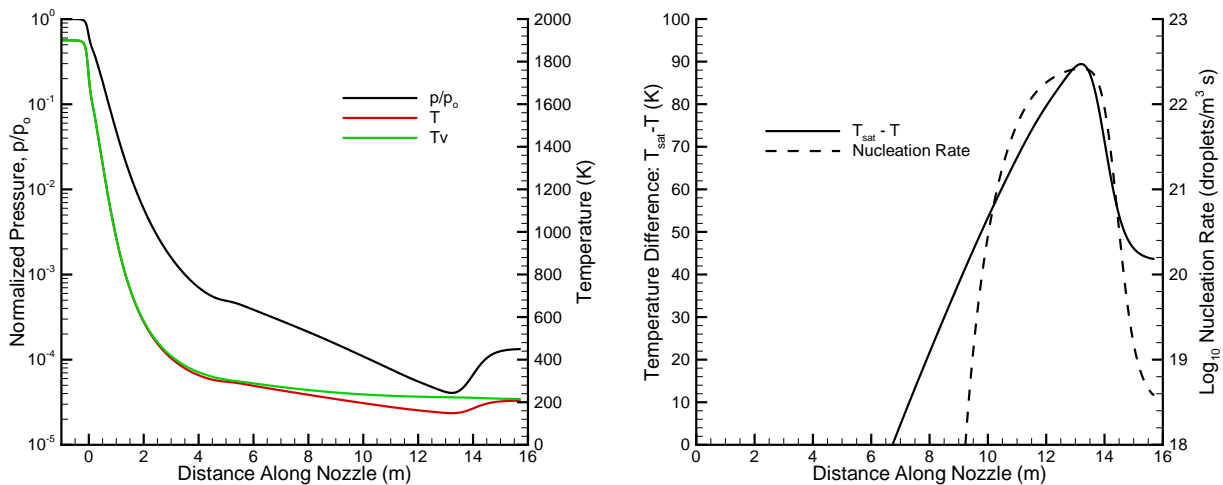

Figure 5.13 – *Computed temperatures and static pressure (left) and supersaturation temperature and nucleation rate (right) on the Langley $8'$ HTT nozzle centerline at Ref. 17 Case 1 test conditions.*

5.5 Summary

A computational fluid dynamics method for the simulation of high-pressure nonequilibrium nozzle flows has been developed and compared to previous simulations and experiments. The gas is modeled with an excluded volume equation of state, which has been shown to be accurate for typical hypersonic nozzle flows of nitrogen and air. Both vibrational equilibrium and finite-rate vibrational relaxation may be modeled, and finite-rate chemical kinetics models may be used. The Spalart-Allmaras one-equation turbulence model with the Catris-Aupoix compressibility correction is used. The code uses a generalized form of flux vector splitting that correctly accounts for the non-ideal equation of state. The time-dependent equations are integrated in time using a parallelizable implicit method which is efficient on the highly stretched grids required to resolve the boundary

layer in high-pressure nozzle flows.

The nozzle simulation code was compared to AEDC Tunnel 9 data and previous simulations of Korte *et al.* (Ref. 39). The present method over-predicts the Pitot pressure for the high pressure case (Run 2209) in comparison to both the previous simulations and the experiments. For the moderate pressure conditions, the code agrees well with the simulations of Ref. 39. It was found that vibrational equilibrium lowers the predicted Pitot pressure slightly (1.4%), though not enough to agree with the measurements. Vibrational equilibrium was modeled in two ways: either with a much faster relaxation rate, or by using an equilibrium caloric equation of state. It was found that both methods produce essentially the same results, allowing equilibrium flows to be simulated with finite-rate code. Simulations of the CUBRC shock tunnel facilities are in excellent with Pitot pressure and nozzle wall heat transfer rate measurements. Reasonable agreement was also obtained in comparisons of hydrocarbon combustion expansion and nucleation in the NASA Langley 8-Foot High Temperature Tunnel.

The reasons for the poor agreement with the high-pressure AEDC Tunnel 9 data are under investigation. The thermo-chemical models are in excellent agreement with accurate thermophysical property data. The primary uncertainty is the turbulence model because it is responsible for producing the correct boundary layer displacement thickness along the entire nozzle during the very rapid expansion. Comparisons with measured Pitot pressure surveys in the nozzle boundary layer are excellent in the near wall region, lending some support to the use of the Spalart-Allmaras turbulence model. Additional work needs to be performed to better understand this discrepancy.

6. References

1. Armaly, B.F., and L. Sutton, "Viscosity of Multicomponent Partially Ionized Gas Mixtures," AIAA 1980-1495, July 1980.

2. Bird, G.A., *Molecular Gas Dynamics*, Clarendon Press, Oxford, 1976.

3. Blottner, F.G., M. Johnson, and M. Ellis, "Chemically Reacting Viscous Flow Program for Multi-Component Gas Mixtures," *Report No. SC-RR-70-754, Sandia Laboratories, Albuquerque, New Mexico,* 1971.

4. Boyd, I.D., G. Chen, and G.V. Candler, "Predicting Failure of the Continuum Fluid Equations in Transitional Hypersonic Flows," *Physics of Fluids,* Vol. 7, No. 1, Jan. 1995, pp. 210-219.

5. Boyd, I.D., D. Karipides, G.V. Candler, and D.A. Levin, "Effect of Dissociation Modeling in Strongly Nonequilibrium Flows at High Altitude," *AIAA Paper No. 95-0709,* Jan. 1995.

6. Burnett, D., "The Distribution of Molecular Velocities and the Mean Motion in a Non-Uniform Gas," *Proc. London Mathematical Soc.,* Vol. 40, 1936, pp. 382.

7. Camac, M., "CO_2 Relaxation Processes in Shock Waves," *Fundamentals of Phenomena in Hypersonic Flows,* edited by J.G. Hall, Cornell Univ. Press, Ithaca, NY, 1966, pp. 195-215.

8. Candler, G.V. and R.W. MacCormack, "The Computation of Hypersonic Ionized Flows in Chemical and Thermal Nonequilibrium," *Journal of Thermophysics and Heat Transfer,* Vol. 5, No. 3, pp. 266-273, July 1991.

9. Candler, G.V., P.K. Subbareddy, and J.M. Brock, "Advances in Computational Fluid Dynamics Methods for Hypersonic Flows," *Journal of Spacecraft and Rockets*, Vol. 52, No. 1, pp. 17-28, Jan.-Feb. 2015.

10. Candler, G.V., "Rate Processes in Hypersonic Flows," forthcoming in *Annual Reviews of Fluid Mechanics.*

11. Catris, S., and B. Aupoix, "Density Corrections for Turbulence Models," *Aerospace Science and Technology,* Vol. 4, 2000, pp. 1-11.

12. Chase M.W. Jr., "NIST-JANAF Thermochemcial Tables, Fourth Edition," *Journal of Physical and Chemical Reference Data,* Monograph 9, 1998.

13. Chaudhry, R.S., *Modeling and Analysis of Chemical Kinetics for Hypersonic Flows in Air,* Ph.D. Thesis, Aerospace Engineering & Mechanics, University of Minnesota, Dec. 2018.

14. Clarke, J.F. and M. McChesney, *Dynamics of Relaxing Gases,* Butterworths, London, 1975.

15. Drayna, T.W., I. Nompelis, and G.V. Candler, "Numerical Simulation of the AEDC Waverider at Mach 8," *AIAA 2006-2816*, June 2006.

16. Druguet, M.C., G.V. Candler, and I. Nompelis, "Effects of Numerics on Navier-Stokes

Computations of Hypersonic Double-Cone Flows," *AIAA Journal*, Vol. 43, No. 3, March 2005, pp. 616-623.

17. Erickson, W.D., G.H. Mall, and R.K. Prabhu, "Finite-Rate Water Condensation in Combustion Heated Wind-Tunnels," NASA TP 2833, 1988.

18. Fay, J.A. and F.R. Riddell, "Theory of Stagnation Point Heat Transfer in Dissociated Air," *J. Aeronautical Sci.* Vol. 25, 1958, pp. 73-85.

19. Gaitonde, D.V., P.W. Canupp, and M.S. Holden, "Heat Transfer Predictions in a Laminar Hypersonic Viscous/Inviscid Interaction," *Journal of Spacecraft and Rockets,* Vol. 16, No. 4, 2002, pp. 481-489.

20. Glowacki, W.J., "NOL Hypervelocity Wind Tunnel Report No. 2: Nozzle Design," NOLTR 71-6, April 1971.

21. Gnoffo, P.A., R.N. Gupta, and J.L. Shinn, "Conservation Equations and Physical Models for Hypersonic Air Flows in Thermal and Chemical Nonequilibrium," NASA TP-2867, 1989.

22. Gökçen, T., "Computation of Hypersonic Low Density Flows with Thermochemical Nonequilibrium," *Ph.D. Thesis,* Department of Aeronautics and Astronautics, Stanford University, June 1989.

23. Gordon, S., and B.J. McBride, "Computer Program for Calculation of Complex Chemical Equilibrium Compositions and Applications, I. Analysis," NASA RP-1311, Oct. 1994.

24. Gosse, R., and G.V. Candler, "Diffusion Flux Modeling: Application to Direct Entry Problems," AIAA 2005-0389, Jan. 2005.

25. Goulard, R., "On Catalytic Recombination Rates in Hypersonic Stagnation Heat Transfer," *Jet Propulsion*, Vol. 28, 1958, pp. 737-745.

26. Graves, R.E., and B.M. Argrow, "Bulk Viscosity: Past to Present," *Journal of Thermophysics and Heat Transfer,* Vol. 13, No.3, 1999, pp. 337-342.

27. GRI-Mech3.0 `http://www.me.berkeley.edu/gri_mech/`

28. Gupta, R.N., J.M. Yos, R.A. Thompson, and K.-P. Lee, "A Review of Reaction Rates and Thermodynamic Transport Properties for an 11-Species Air Model for Chemical and Thermal Nonequilibrium Calculations to $30,000\,\mathrm{K}$," *NASA RP-1232,* Aug. 1990.

29. Hassan, B., G.V. Candler, and D.R. Olynick, "Thermo-Chemical Nonequilibrium Effects on the Aerothermodynamics of Aerobraking Vehicles," *Journal of Spacecraft and Rockets,* Vol. 30, No. 6, Nov.-Dec. 1993, pp. 647-655.

30. Heims, S.P., "Moment Equations for Vibrational Relaxation Coupled with Dissociation," *J. Chem. Phys.,* Vol. 38, 1963, pp. 603.

31. Holden, M.S., T.P. Wadhams, J.K. Harvey, G.V. Candler, "Comparisons Between DSMC and Navier-Stokes Solutions on Measurements in Regions of Laminar Shock Boundary Layer Interaction in Hypersonic Flows," *AIAA-2002-0435,* Jan. 2002.

32. Jacobsen, R.T., Stewart, R.B., McCarty, R.D., and Hanley, H.J.M., "Thermophys-

ical Properties of Nitrogen from the Fusion Line to 3500 R (1944 K) for Pressures to 150,000 psia (10342×10^5 N/m^2)," National Bureau of Standards, NBS TN 648, Boulder, CO, Dec. 1973.

33. Johnson, H.B., T.G. Seipp, and G.V. Candler, "Numerical Study of Hypersonic Reacting Boundary Layer Transition on Cones," *Physics of Fluids,* Vol. 10, No. 10, pp. 2676-2685, Oct. 1998. Also *AIAA Paper No. 97-2567,* June 1997.

34. Jones, K.M., *Boundary Layer Study on Nozzle Wall at Hypersonic Velocities,* Ph.D. Thesis, North Carolina State University, 1992.

35. Kim, S.-E., B. Makarov, and D. Careani, "A Multi-Dimensional Linear Reconstruction Scheme for Arbitrary Unstructured Grids," AIAA Paper 2003-3990, June 2003.

36. Knab, O., H.-H. Frühauf, and S. Jonas, "Multiple Temperature Descriptions of Reaction Rate Constants with Regard to Consistent Chemical-Vibrational Coupling," *AIAA Paper No. 92-2947,* July 1992.

37. Knab, O., H.-H. Frühauf, and E.W. Messerschmid, "Validation of a Physically Consistent Coupled Chemical-Vibrational Model for Ionized Air in Thermo-Chemical Nonequilibrium," *AIAA Paper No. 93-2866,* July 1993.

38. Knab, O., T.H. Gogel, H.-H. Frühauf, and E.W. Messerschmid, "CVCV Model Validation by Means of Radiative Heating Calculations," *AIAA Paper No. 95-0623,* Jan. 1995.

39. Korte, J.J., E. Hedlund, and S. Anandakrishnan, "A Comparison of Experimental Data With CFD For NSWC Hypervelocity Wind Tunnel 9 Mach 14 Nozzle," AIAA Paper 92-4010, July 1992.

40. Landau, L. and E. Teller, "Theory of Sound Dispersion," Physikalische Zeitschrift der Sowjetunion, Vol. 10, No. 34, 1936.

41. Lee, J.H., "Basic Governing Equations for the Flight Regimes of Aeroassisted Orbital Transfer Vehicles," *Thermal Design of Aeroassisted Orbital Transfer Vehicles,* ed. H.F. Nelson, *Progress in Aeronautics and Astronautics,* Vol. 96, 1985, pp. 3-53.

42. Lee, J.H. "Electron-Impact Vibrational Excitation Rates in the Flowfield of of Aeroassisted Orbital Transfer Vehicles," *Thermophysical Aspects of Re-entry Flows,* eds. J.N. Moss and C.D. Scott, *Progress in Aeronautics and Astronautics,* Vol. 103, 1986, pp. 197-224.

43. Lemmon, E.W., R.T. Jacobsen, S.G. Penoncello, D.G. Friend, "Thermodynamic Properties of Air and Mixtures of Nitrogen, Argon, and Oxygen from 60 to 2000 K at Pressures to 2000 MPa," *J. Phys. Chem. Ref. Data,* Vol. 29, No. 3, 2000, pp. 331-385.

44. Levin, E., and M.J. Wright, "Collision Integrals for Ion-Neutral Interactions of Nitrogen and Oxygen," *Journal of Thermophysics and Heat Transfer,* Vol. 18, No. 1, 2004, pp. 143-147.

45. Liou, M.S., B. Van Leer, and J.S. Shuen, "Splitting of Fluxes for Real Gases," NASA TM-100856, Apr. 1988.

46. Liou, M.S., B. Van Leer, and J.S. Shuen, "Splitting of Inviscid Fluxes for Real Gas,"

J. Comp. Phys., Vol. 87, 1990, pp. 1-24.

47. Lordi, J.A., and R.E. Mates, "Nonequilibrium Expansions of High-Enthalpy Flows," Aerospace Research Laboratories, ARL 64-206, Buffalo, NY, Nov. 1964.

48. Lumpkin, F. E., III and D.R. Chapman, "Accuracy of the Burnett Equations for Hypersonic Real Gas Flows," *J. Thermophysics and Heat Transfer*, Vol. 6, No. 3, July-Sept. 1992, pp. 419-425.

49. MacCormack, R.W., "Current Status of the Numerical Solutions of the Navier-Stokes Equations," *AIAA Paper No. 85-0032,* Jan. 1985.

50. MacCormack, R.W. and G.V. Candler, "The Solution of the Navier-Stokes Equations Gauss-Seidel Line Relaxation," *Computers and Fluids*, Vol. 17, No. 1, 1989, pp. 135-150.

51. MacCormack, R.W., "Solution of the Navier-Stokes Equations in Three Dimensions," *AIAA Paper No. 90-1520,* June 1990.

52. MacCormack, R.W., *Numerical Computation of Compressible and Viscous Flow,* AIAA Education Series, 2014.

53. Macheret, S.O. and J.W. Rich, "Nonequilibrium Dissociation Rates Behind Strong Shock Waves: Classical Model," *J. Chem. Phys.,* Vol. 174, 1993, pp. 25.

54. MacLean, M., G.V. Candler, and M.S. Holden, "Numerical Evaluation of Flow Conditions in the LENS Reflected Shock-Tunnel Facilities," AIAA Paper 2005-0903, Jan. 2005.

55. Marrone, P.V. and C.E. Treanor, "Chemical Relaxation With Preferential Dissociation from Excited Vibrational Levels," *Physics of Fluids,* Vol. 6, 1963, pp. 1215-1221.

56. Mavriplis, D., "Revisiting the Least-Squares Procedure for Gradient Reconstruction on Unstructured Meshes," NASA Report CR-2003-212683, Dec. 2003.

57. Millikan, R.C. and D.R. White, "Systematics of Vibrational Relaxation," *J. Chem. Phys.,* Vol. 39, 1963, pp. 3209-3213.

58. Nompelis, I., G.V. Candler, and M.S. Holden, "Effect of Vibrational Nonequilibrium on Hypersonic Double-Cone Experiments," *AIAA Journal,* Vol. 41, No. 11, Nov. 2003, pp. 2162-2169.

59. Olejniczak, J., G.V. Candler, H.G. Hornung, and C. Wen, "Experimental Evaluation of Vibration-Dissociation Coupling Models," *AIAA Paper No. 94-1983,* June 1994.

60. Olejniczak, J., and G.V. Candler, "Vibrational Energy Conservation with Vibration-Dissociation Coupling: General Theory and Numerical Studies," *Physics of Fluids,* Vol. 7, No. 7, July 1995, pp. 1764-1774.

61. Palmer, G., and M.J. Wright, "Comparison of Methods to Compute High-Temperature Gas Viscosity," *Journal of Thermophysics and Heat Transfer,* Vol. 17, No. 2, 2003, pp. 232-239.

62. Palmer, G., and M.J. Wright, "Comparison of Methods to Compute High-Temperature Gas Thermal Conductivity," AIAA 2003-3913, June 2003.

63. Park, C., "On Convergence of Computation of Chemically Reacting Flows," *AIAA Paper No. 85-0247,* Jan. 1985.

64. Park, C., "Calculation of Nonequilibrium Radiation in the Flight Regimes of Aeroassisted Orbital Transfer Vehicles. *Thermal Design of Aeroassisted Orbital Transfer Vehicles,* ed. H.F. Nelson, *Progress in Aeronautics and Astronautics,* Vol. 96, 1985, pp. 395-418.

65. Park, C., "Problems of Rate Chemistry in the Flight Regimes of Aeroassisted Orbital Transfer Vehicles. *Thermal Design of Aeroassisted Orbital Transfer Vehicles,* ed. H.F. Nelson, *Progress in Aeronautics and Astronautics,* Vol. 96, 1985, pp. 511-537.

66. Park, C., "Assessment of Two-Temperature Kinetic Model for Dissociating and Weakly Ionizing Nitrogen," *AIAA Paper No. 86-1347,* June 1986.

67. Park, C., "Assessment of Two-Temperature Kinetic Model for Ionizing Air," *AIAA Paper No. 87-1574,* June 1987.

68. Park, C., *Nonequilibrium Hypersonic Aerothermodynamics,* Wiley, 1990.

69. Park, C., "Review of Chemical-Kinetic Problems of Future NASA Missions, I: Earth Entries," *Journal of Thermophysics and Heat Transfer,* Vol. 7, No. 3, July-Sept. 1993, pp. 385-398.

70. Park, C., J.T. Howe, R.L. Jaffe, and G.V. Candler, "Review of Chemical-Kinetic Problems of Future NASA Missions, II: Mars Entries," *Journal of Thermophysics and Heat Transfer,* Vol. 8, No. 1, Jan.-Mar. 1994, pp. 9-23.

71. Peterson, D., and G.V. Candler, "Detached Eddy Simulation of RCS-Aerodynamic Interaction of Mars Science Laboratory Capsule," *AIAA-2008-624,* Jan. 2008.

72. Ramshaw, J.D., "Self-Consistent Effective Binary Diffusion in Multicomponent Gas Mixtures," *Journal of Non-Equilibrium Thermodynamics,* Vol. 15, No. 3, 1990, pp. 295-300.

73. Ramshaw, J.D., and C.H. Chang, "Friction Weighted Self-Consistent Effective Binary Diffusion Approximation," *Journal of Non-Equilibrium Thermodynamics,* Vol. 21, No. 3, 1996, pp. 223-232.

74. Ramshaw, J.D., and C.H. Chang, "Ambipolar Diffusion in Two-Temperature Multicomponent Plasmas," *Plasma Chemistry and Plasma Processing,* Vol. 13, No. 3, 1993.

75. Resler, E.L., Jr., "Characteristics and Sound Speed in Nonisentropic Gas Flows with Nonequilibrium Thermodynamic States," *Journal of the Aeronautical Sciences,* Vol. 24, No. 11, Nov. 1957, pp. 785-790.

76. Smith, M.S., and J.J. Coblish, "Measurements to Assess the Degree of Thermal Nonequilibrium at AEDC Hypervelocity Wind Tunnel No. 9," AIAA Paper 2004-2399, June 2004.

77. Spalart, P.R., and Allmaras, S.R., "A One-Equation Turbulence Model for Aerodynamic Flows," AIAA Paper 92-0439, Jan. 1992.

78. Spalart, P.R., Jou, W-H., Strelets, M., and Allmaras, S.R., "Comments on the Feasi-

bility of LES for Wings, and on a Hybrid RANS/LES Approach, Advances in DNS/LES, 1st AFOSR Int. Conf. On DNS/LES, Greyden Press, Columbus, OH, 1997.

79. Steger, J. and R.W. Warming, "Flux Vector Splitting of the Inviscid Gasdynamics Equations with Application to Finite Difference Methods," *NASA TM-78605*, 1979.

80. Thompson, P.A., *Compressible-Fluid Dynamics,* McGraw-Hill, NY 1971, pp. 95-102.

81. Treanor, C.E. and P.V. Marrone, "Effect of Dissociation on the Rate of Vibrational Relaxation," *Physics of Fluids,* Vol. 5, 1962, pp. 1022-1026.

82. van Leer, B., "Towards the Ultimate Conservative Difference Scheme, V: A Second-Order Sequel to Godunov's Method," *Journal of Computational Physics,* Vol. 32, 1979, pp. 101-136.

83. Vincenti, W.G. and C.H. Kruger, Jr., *Introduction to Physical Gas Dynamics,* Krieger Publishing Company, Florida, 1965.

84. Wilke, C.R., "A Viscosity Equation for Gas Mixtures," *J. Chem. Phys.,* Vol. 18, 1950, pp. 517-519.

85. Wright, M.J., M. Prampolini, and G.V. Candler, "Data Parallel Lower-Upper Relaxation Method for the Navier-Stokes Equations," *AIAA Journal,* Vol. 34, No. 7, 1996, pp. 1371-1377.

86. Wright, M.J., D. Bose, and G.V. Candler, "A Data-Parallel Line Relaxation Method for the Navier-Stokes Equations," *AIAA Journal,* Vol. 36, No. 9, 1998, pp. 1603-1609.

87. Wright, M.J., E. Levin, "Collision Integrals for Ion-Neutral Interactions of Air and Argon," *Journal of Thermophysics and Heat Transfer,* Vol. 19, No. 1, 2005, pp. 127-128.

88. Wright, M.J., D. Bose, G.E. Palmer, E. Levin, "Recommended Collision Integrals for Transport Property Computations Part 1: Air Species," *AIAA Journal,* Vol. 43, No. 12, 2005, pp. 2558-2564.

89. Wright, M.J., H.H. Hwang, and D.W. Schwenke, "Recommended Collision Integrals for Transport Property Computations Part II: Mars and Venus Entries," *AIAA Journal,* Vol. 45, No. 1, 2007, pp. 281-288.

90. Yee, H.C., "A Class of High-Resolution Explicit and Implicit Shock-Capturing Methods," *NASA TM-101088,* Feb. 1989.

91. Zhong, X., R.W. MacCormack, and D.R. Chapman, "Stabilization of the Burnett Equations and Applications to Hypersonic Flows. *AIAA J.,* Vol. 31, 1993, pp. 1036.